Tsunami wave interaction with mangrove forests: a 3-D numerical approach

Maria Maza, Javier L. Lara and Inigo J. Losada

Environmental Hydraulics Institute "IH Cantabria". Universidad de Cantabria. C/Isabel Torres nº15

Parque Científico y Tecnológico de Cantabria 39011 Santander. Spain.

A three dimensional numerical approach based on IHFOAM to study the interaction of tsunami waves with mangrove forest is presented. As a first approximation, the problem is modelled by means of solitary waves impinging on emergent rigid cylinders. Two different conceptual approaches are implemented into IHFOAM. Solving the URANS equations provides a direct simulation of the flow field considering the actual geometry of the array of cylinders. A modified version of the volume-average URANS equations by introducing a drag force to model the momentum damping created by the cylinders is used in the second approach. Both the direct and macroscopic simulations are validated against laboratory experiments for wave damping with very high agreement. A large set of numerical experiments to analyse flow parameters and uniform and random cylinder array distributions are analysed and use to compare pros and cons of the different approaches. Large differences are found in the forces exerted on the vegetation for uniform and random distributions. Generalizations obtained from uniform arrangements could lead to underestimation of wave-exerted forces, especially for low dense configurations. Wave forces calculated with the macroscopic approach by means of the drag coefficient yields clear underestimations.

Keywords: rigid vegetation, solitary wave, 3-D URANS model, wave forces, drag coefficient

1. Introduction

Different authors have pointed out that mangrove forests provide coastal protection. Shuto (1987) quantitatively estimated the effectiveness of coastal pine forests in Japan against tsunami by statistically analysing the physical damage suffered by the trees. After the December 2004 tsunami, Kandasamy and Narayanasamy (2005) performed a study in 18 coastal hamlets along the southeast coast of India highlighting the importance of mangrove forests in coastal area protection. Following with this idea several authors (e.g. Mazda et al., 2006; Tanaka et al., 2007; Vo-Luong and Massel, 2008) reported the human and economic damage reduction produced at places where dense mangrove forests were present in comparison with bare sand areas.

Since mangrove capacity attenuating tsunami waves has been proven, many authors have focused on assessing tsunami wave attenuation and flow patterns around the plants. Due to the complexity of the problem, physical models have been frequently used to determine dissipation capacity of mangroves. Many of these studies have been carried out using simplified vegetation models, such us cylinders, disposed in uniform and organized

arrangements. Huang et al. (2011) performed a set of runs to study wave evolution along three different cylinder arrangements and different field widths. Also Irtem et al. (2009) tested cylindrical timber sticks to study tsunami run-up reduction. The same runs where performed considering artificial trees. Authors pointed out the necessity of future studies where different types of trees are considered for random horizontal distributions. In the last years, different authors have used more sophisticated plant models. Ismail et al. (2012) tested prototype Rhizophora mangrove forests formed by three different parts: canopy, trunk and root. They showed the strong influence of forest density and width on wave damping. Strusinska et al. (2013) also reproduced Rhizophora species developing a novel tree parameterization, which accounts for both biomechanical and structural tree properties. Both solitary waves and tsunami bores were tested and similar wave damping was recorded for both flow conditions. They also pointed out that the highest forces were always measured at the first trees row and their magnitude was independent of the forest length. Another aspect studied was the importance of wave incident characteristics in their propagation along the vegetation patch. All these experimental studies reported the capacity of mangrove forests on attenuating wave energy and the complex processes produced in the interaction of tsunami waves with vegetation fields, such as the wave height enhancement at the seaward edge of the mangrove forest or the nonlinear wave damping behaviour. Moreover, such studies also pointed out different limitations and gaps, such as scale effects, vegetation parameterization, flow conditions modelling, plants horizontal distribution or constraints in physical space that must be considered and covered in future studies.

In recent years, numerical approaches have been also developed to predict and to reproduce the effect that mangrove forests have on tsunami wave propagation. Most of these numerical models are based on shallow water two-dimensional vertical averaged equations. Teh et al. (2009) introduced the Morison equation in a model based on the Boussinesq equations considering the drag and the inertia coefficients as calibration parameters. They used the formulas proposed by Harada and Imamura (2003) for these coefficients, which were based upon data collected on coastal pine forest in Japan. Formulations were quantified as a function of the volume of trees under the water surface within a chosen control volume. More recently, Suzuki et al. (2011) implemented Mendez et al. (2004) formulation in the SWAN model to reproduce wave dissipation over vegetation fields. They included a vertical layer schematization for vegetation with variable vertical area such as mangroves. However, Mendez et al. (2004) was determined for submerged seaweed, far from the biomechanics properties of rigid mangrove forest. These models allow obtaining an estimation of wave damping produced by mangrove forests but they are based on empirical coefficients, which need to be calibrated to achieve realistic results. In addition they are not able to solve the vertical distribution of the velocity field or to deal with high turbulence flows. Another important limitation is the prediction of the pressure field, which is far from a hydrostatic behaviour, especially for bore-type tsunami waves. These aspects can be critical in the estimation of the protection provided by a mangrove forest.

More recently, the use of the Navier-Stokes (NS) equations has been applied with the main motivation of getting a better flow representation to improve the understanding of dissipation mechanisms induced by vegetation (i.e.: Maza et al., 2013). Models based on NS equations allow simulating flow vertical components and the flow between individual elements

considering appropriate turbulence effects. As a first approximation, Mei et al. (2013) presented a semi-analytical theory of wave propagation through vegetated water based on a linearized version of the NS equations. The model extended the solution presented for long waves in Mei et al. (2011) to consider waves of intermediate period and length. Both works present a model able to simulate the micro-scale flow modelling around idealized rigid vegetation formed by cylinders, to determine macro-scale properties. One of the limitations of that approach is that the solution can cover only linear solutions although reasonable results are also found out of the range of applicability for waves of intermediate length. With the same spirit, the use of a numerical model based on the complete NS equations is used in this work. The combination of two approaches is presented, the first is based on a microscopic simulation of the flow around the vegetation whereas the second takes advantages of a macroscopic definition of the flow by means of the wave damping parameterization. The modelling presented here increases the range of applicability of Mei et al. (2013) approach considering the complete version of the NS equations. The limitations in the flow modelling derived from the use of a simplified macroscopic approach will be investigated.

The work is organized as follows. First, the mathematical description of the model is presented for both approaches, macro- and microscopic modelling. Model validation is carried out next, using laboratory experiments. Next section includes additional simulations carried out aiming at studying the influence of solitary wave steepness, vegetation density and vegetation arrangement on the tsunami wave attenuation and the forces exerted on the plants. A discussion on the differences in the flow induced forces and wave damping is included.

2. Mathematical modelling

Two different approaches have been followed to simulate tsunami wave interaction with mangrove forest. First, direct simulation of the wave induced flow field around the vegetation is carried out using the Unsteady Reynolds-Averaged Navier-Stokes (URANS) equations. The flow within the mangrove forest is resolved considering the individual cylinder actual geometry. A standard $\kappa - \omega$ SST model is included as the turbulence closure, due to its ability to deal with reverse pressure gradients that are developed around rigid cylinders (Menter, 1994). This approach could be understood as a direct simulation considering that the flow is resolved at the space between cylinders. The second mathematical approach is focused on a macroscopic representation of the flow field within the vegetation. A simplification of a standard Volume-Averaged URANS (VARANS) set of equations presented in del Jesus et al. (2012) and Higuera et al. (2014) is used. The model first presented by Maza et al. (2013) neglects the role played by the porosity of the field resolving the flow as a combination of a drag force, to represent wave damping, and a modified $\kappa - \boldsymbol{\varepsilon}$ turbulence model, used to consider enhanced turbulence by vegetation. Comparisons of flow velocities within the vegetation field by Maza et al. (2013) demonstrate the accuracy of this approach to reproduce flow characteristics for high-density vegetation fields.

2.1. Numerical model description.

IHFOAM model (Higuera et al., 2013a) is used in the first approach for direct simulation of the wave induced flow field around the vegetation. IHFOAM is a three-dimensional Navier-Stokes (NS) solver built on the OpenFOAM platform. The model uses a modified version of the OpenFOAM standard "interFoam" solver. IHFOAM allows simulating gravity waves (Higuera et al, 2013a, 2013b) and porous media flows (Higuera et al, 2014a, 2014b). It also incorporates a set of algorithms to generate and absorb waves at the boundaries without the use of relaxation zones, speeding-up the simulations and ensuring a correct representation of the wave-induced hydrodynamics in the numerical domain.

The aforementioned NS equations, which include continuity (Eq. (1)) and momentum conservation (Eq. (2)) equations, are the governing mathematical formulations for free surface flows, linking fluid pressure and fluid velocity. The assumption of incompressible fluids applies for most coastal engineering problems.

$$\frac{\partial \overline{u}_i}{\partial x_i} = 0 \tag{1}$$

$$\frac{\partial \rho \overline{u}_i}{\partial t} + \overline{u}_j \frac{\partial \rho \overline{u}_i}{\partial x_j} - \frac{\partial}{\partial x_j}\left(\mu_{eff} \frac{\partial \overline{u}_i}{\partial x_j}\right) = \frac{\partial p^*}{\partial x_i} - g_i x_j \frac{\partial \rho}{\partial x_j} \tag{2}$$

In equations (1) and (2) ρ is density calculated as $\rho = \alpha \rho_{water} + (1-\alpha)\rho_{air}$ where α is the single phase function according to equation (3) and ρ_{water} and ρ_{air} are the water and air densities; p* is the pseudo-dynamic pressure; x_i is the Cartesian position vector with respect to the reference frame (x_1, x_2, x_3); $\overline{u}_i$ are the fluid velocity components $(\overline{u}_1, \overline{u}_2, \overline{u}_3)$ regarding the Cartesian system of coordinates; g_i is the acceleration of gravity which is acting along the vertical axis ($g_1 = 0$, $g_2 = 0$, $g_3 = g$) and μ_{eff} is the efficient dynamic viscosity, which takes into account the molecular dynamic viscosity plus the turbulent effects: $\mu_{eff} = \mu + \rho \nu_t$. The newly introduced ν_{turb} is the turbulent kinetic viscosity, obtained from the turbulence modelling. This solver supports several turbulence models (e.g. $\kappa - \boldsymbol{\varepsilon}$, $\kappa - \omega$ SST, and LES), however only $\kappa - \omega$ SST is considered in this work.

An additional equation (Eq. (3)) must also be taken into account to describe the movement of the air and water phases. IHFOAM solver considers only a single phase function (α), defined as the quantity of water per unit of volume at each cell. This means that if $\alpha = 1$ the cell is full of water, if $\alpha = 0$ the cell is full of air, and in any other case it belongs to the interface. Phase movement is described by the following equation:

$$\frac{\partial \alpha}{\partial t} + \frac{\partial \overline{u}_i \alpha}{\partial x_i} - \frac{\partial \overline{u}_{c,i} \alpha (1-\alpha)}{\partial x_i} = 0 \tag{3}$$

in which $\overline{u}_{c,i}$ is an artificial compression term used to preserve a sharp interface between air and water calculated as $\overline{u}_{c,i} = min(C_\alpha |\overline{u}_i| \; at \; x_i, max(|\overline{u}_i|) \; \forall \; x_i at \; free \; surface)$ where C_α is

a factor specified by the user (by default equal to 1). This term is evaluated individually for each volume. The first term is calculated considering the velocity at each individual finite volume and the second term considers the maximum of the velocity in every volume in the domain being part of the free surface ($\alpha < 1$). This term has been widely used (e.g.: Weller et al., 1998; Rusche, 2002; Higuera et al. 2013a) and it is standard in the two-phase flow solver available in OpenFOAM.

In order to study the tsunami wave interaction with mangrove forests using a macroscopic approach, IHFOAM needs some modifications. A second approach is proposed here by volume averaging the URANS equations presented in (1) and (2). It relies on obtaining a mean behavior of the flow within the vegetation by averaging its properties over control volumes. Volume averaging NS equations allows representing the vegetated area as a continuous medium, defined by its macroscopic properties only and considering the coupling of the velocity and pressure fields, inside and outside the vegetation. Hence, it allows eliminating the need of a detailed description of its complex geometry, as in the first approach and a speed-up of the calculations, because coarser grids can be used. This simplification, however, introduces new terms in the equations (del Jesus et al., 2012 and Higuera et al., 2014) that need to be modeled, such as the drag and the inertia forces. In the present work a simplification has been followed due to the specific characteristics of vegetation, which exhibit high porosity values. Equations presented for porous media flow by del Jesus et al. (2012) and Higuera et al. (2014) are adapted neglecting the role played by porosity on fluid acceleration (both local and convective). This approach is not new and has been successfully applied to flow interacting with vegetation using both a RANS turbulence approach (Hiraoka et al., 2006 for steam flow and Maza et al., 2013 for wave flow) or Dupont et al. (2010) for air flow by means of LES modeling of the turbulent flow. Equations (1) and (2) are then modified by considering the volume averaged as follows:

$$\frac{\partial \langle \overline{u}_i \rangle}{\partial x_i} = 0 \tag{4}$$

$$\frac{\partial \rho \langle \overline{u}_i \rangle}{\partial t} + \langle \overline{u}_j \rangle \frac{\partial \rho \langle \overline{u}_i \rangle}{\partial x_j} - \frac{\partial}{\partial x_j}\left(\langle \mu_{eff} \rangle \frac{\partial \langle \overline{u}_i \rangle}{\partial x_j} \right) = \frac{\partial \langle p^* \rangle}{\partial x_i} - g_i x_j \frac{\partial \langle \rho \rangle}{\partial x_j} - \overline{F_{D,\,i}} - \overline{F_{I,\,i}} \tag{5}$$

where $\langle \overline{u}_i \rangle$ is the volume average velocity, $\langle \mu_{eff} \rangle$ is the volume averaged efficient viscosity, $\langle p^* \rangle$ is the volume averaged pseudo-dynamic pressure, $\langle \rho \rangle$ is the volume averaged density, $\overline{F_{D,\,i}}$ is the drag force and $\overline{F_{I,\,i}}$ is the inertia force. The drag force and the inertia force, which account for loss of momentum induced by the plants are modelled as follows:

$$\overline{F_{D,\,i}} = \frac{1}{2} \langle \rho \rangle C_D a N \langle \overline{u}_i \rangle |\langle \overline{u}_i \rangle| \tag{6}$$

$$\overline{F_{I,\,i}} = \langle \rho \rangle C_M \frac{\pi a^2}{4} N \frac{\partial \langle \overline{u}_i \rangle}{\partial t} \tag{7}$$

Where a is the width of the vegetation element, C_D is the drag coefficient, N is the number of plants per unit area and C_M is the inertia coefficient which is equal to $C_M = C_m + 1$ where C_m is considered equal to 1 (Sumer and Fredsoe, 2006). In this approach, the flow field between

the vegetation elements is not resolved. Turbulence modelling is carried out by means of a modified k-**ε** model for wave flow (Maza et al., 2013). The presence of vegetation is considered by adding a source energy production term, k_w, and sink energy dissipation term, ε_w, in the traditional κ − **ε** turbulence model. These terms take into account the turbulence enhancement by vegetation. These two additional terms are included in the turbulence model as:

$$\frac{\partial k}{\partial t} + \langle \bar{u}_j \rangle \frac{\partial k}{\partial x_j} = \frac{\partial}{\partial x_j}\left[\langle \nu_{eff} \rangle \frac{\partial k}{\partial x_j}\right] + \langle \nu_t \rangle \frac{\partial \langle \bar{u}_i \rangle}{\partial x_j}\left(\frac{\partial \langle \bar{u}_i \rangle}{\partial x_j} + \frac{\partial \langle \bar{u}_j \rangle}{\partial x_i}\right) - \varepsilon + \underbrace{C_{kp} C_D a N \sqrt{\langle \bar{u}_j \rangle \langle \bar{u}_j \rangle} k}_{k_w} \quad (8)$$

$$\frac{\partial \varepsilon}{\partial t} + \langle \bar{u}_j \rangle \frac{\partial \varepsilon}{\partial x_j} = \frac{\partial}{\partial x_j}\left[\left(\frac{\langle \nu_t \rangle}{\sigma_\varepsilon} + \langle \nu \rangle\right) \frac{\partial \varepsilon}{\partial x_j}\right] + C_{\varepsilon 1} \frac{\varepsilon}{k} \langle \nu_t \rangle \frac{\partial \langle \bar{u}_i \rangle}{\partial x_j}\left(\frac{\partial \langle \bar{u}_i \rangle}{\partial x_j} + \frac{\partial \langle \bar{u}_j \rangle}{\partial x_i}\right) - C_{\varepsilon 2} \frac{\varepsilon^2}{k} + \underbrace{C_{\varepsilon p} C_D a N \sqrt{\langle \bar{u}_j \rangle \langle \bar{u}_j \rangle} \varepsilon}_{\varepsilon_w} \quad (9)$$

where k is the turbulent kinetic energy, ε the turbulent dissipation rate, $\langle \nu_{eff} \rangle = \langle \nu \rangle + \langle \nu_t \rangle$ and $\langle \nu_t \rangle = C_\mu \frac{k^2}{\varepsilon}$. C_μ , $C_{\varepsilon 1}$, $C_{\varepsilon 2}$ and σ_ε are closure coefficients with values 0.09, 1.44, 1.92 and 1.3 respectively. Values given by Hiraoka et al. (2006) for the new empirical constants C_{kp} and $C_{\varepsilon p}$ are used ($C_{kp} = 1$ and $C_{\varepsilon p} = 3.5$). These coefficients are kept constant for all the simulations in this work.

Inflow boundary conditions have been established following Higuera et al. (2013), which takes into account the generation at the inflow boundaries and the wave absorption at the outflow boundaries by means of Dirichlet boundary conditions, instead relaxation zones. Velocity field is defined attending to the solitary wave characteristics tested in Huang et al. (2011). Non-slip boundary condition is considered at the bottom, at side boundaries and at the cylinder surface. A log-law is considered as a boundary condition for the k- **ε** turbulence model for solid walls (cylinder, bottom and flume sides). Values for the k-ω SST turbulence model used in the first approach are set, according to Menter (1992). Initial values for turbulence in both approaches are defined according to Wilcox (2006). The upper boundary is considered open to air where an atmospheric pressure value is set.

3. Validation

IHFOAM has been validated for both the direct simulation and the macroscopic approaches. Laboratory tests performed by Huang et al. (2011) have been found suitable because they present solitary wave evolution along an idealized mangrove forest built with emergent vertical cylinders. Experimental information on flow characteristics or wave-induced forces on the array of cylinders is unfortunately lacking, and only free surface evolution is used to show model performance.

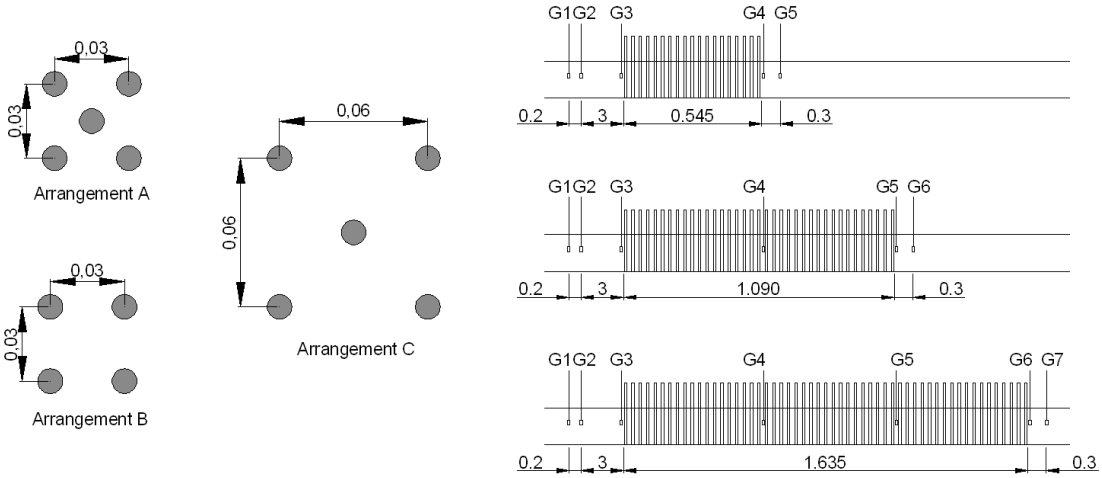

Figure 1. Cylinders arrangements (left) and field length (right).

Huang et al. (2011) present different tests in a 32 m long and 0.55 m wide wave flume using emergent 0.01m-cylinders made of Perspex. They were arranged following three different configurations, A, B and C, with densities equal to N = 2228, 1108 and 560 cylinders/m^2, respectively (Figure 1). Three field lengths l = 0.545, 1.090 and 1.635m were considered, as can be seen in Figure 1. All tests were run considering a water depth equal to h = 0.15m. Solitary wave height was varied from H = 0.02 to 0.06m during the experiments.

Validation for the macro-scale modelling has been focused on the determination of the drag coefficient value, C_D. A fitting procedure is conducted to find the best C_D for modelling the wave induced damping. Both the wave height evolution and the free surface profiles along the vegetation are considered to best represent the quality of the experiments.

Validation for the direct simulation approach is carried out with a detailed simulation of the complete array of cylinders. Each individual cylinder has been considered in the numerical domain. In this case, no empirical coefficients have been used to reproduce experimental measurements. Only standard coefficients from the $\kappa - \omega$ SST are used that remain unchanged for all simulations. The advantage of the second approach is the absence of calibration of the empirical parameters to reproduce the physical processes. However, the computational cost increases, as it will be discussed later.

3.1. Macroscopic approach

The computational domain is defined considering the same geometrical characteristics of the physical wave flume. A non-constant grid-sized and three-dimensional mesh is considered. The discretization is 0.02m in both horizontal directions and 0.006m in the vertical direction. The mesh is refined near the mean water level in order to improve free surface resolution. Values of 0.01m in the horizontal and 0.003m in the vertical directions are considered. Sensitivity to grid size has been tested (not shown here) with negligible differences observed within values close to the ones selected.

Wave generation in the model has been targeted to obtain the same solitary wave in the first free surface gauge as the one measured by Huang et al. (2011) to ensure the same incident wave conditions to model wave damping by vegetation. Wave absorption is set at the onshore boundary in order to absorb outgoing waves. Numerical simulations are carried out attending to the different vegetation arrangements and vegetation densities considered during the experiments, in order to determine the drag force (see Eq. (5)). Drag coefficient, C_D, is the only calibration parameter varied to adjust wave damping in the numerical simulations to measurements.

The first simulation is performed considering the longest vegetation field (l = 1.635m) with the lowest vegetation density (N = 560cylinders/m^2). Figure 2 shows both numerical model results and laboratory measurements for an incident wave height of 0.05m. In this case, the best-fitting drag coefficient is 1.52, the same as presented by Huang et al. (2011) (see Table 1). In this work, the best-fit values for drag coefficients are such that the difference between the maximum free surface elevation of the experimental and numerical data at the gauge located leeward the cylinder field is a minimum. That value is lower than 5% in all cases analysed. As can be observed in the figure, the model reproduces very well the wave height transformation along the vegetation field.

Previous studies such as Mendez and Losada (2004) and Ma et al. (2013) have neglected the inertia force in this approach. In order to analyse this hypothesis Figure 2 shows the numerical free surface evolution with and without considering the inertia force contribution.

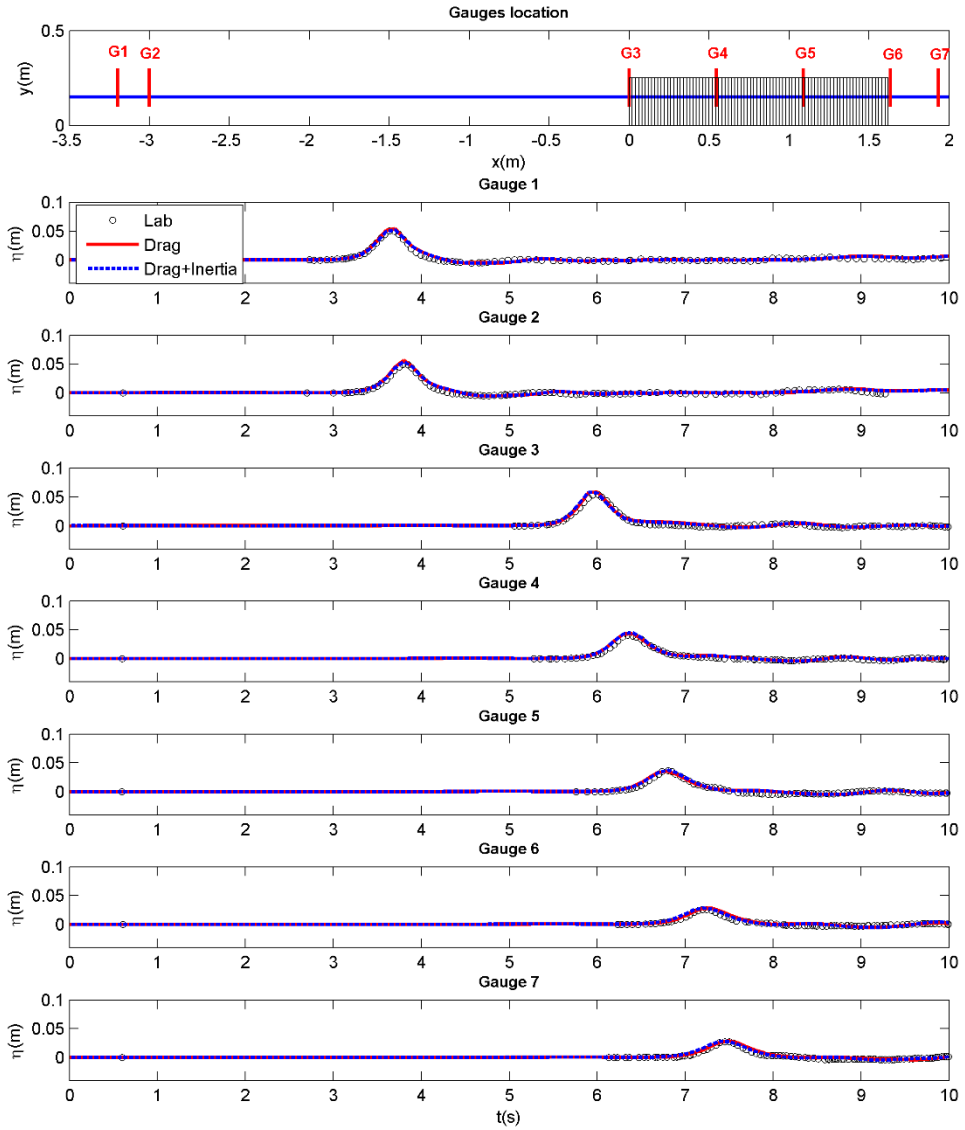

Figure 2. Comparison between numerical and laboratory free surface evolution for arrangement C and vegetation length 1.635m for an incident wave height equal to 0.05m. Numerical results considering drag and inertia forces (dashed blue line) and only drag force (red).

As can be seen results show that, for this case, both numerical results are almost identical, what can be interpreted as an almost negligible contribution from the inertia component. In order to find an explanation the Keulegan-Carpenter number of the flow is calculated considering a solitary wave length equal to $2.12h/\sqrt{H/2h}$ (Dean and Dalrymple, 1991) and its corresponding wave period. For all cases considered in these experiments KC numbers vary between 88 and 106, that is within the range where drag force is dominant (Chakrabarti, 1987). Based on the numerical experiment and the evaluation of the KC range, the inertia force contribution in the rest of the simulations considering the macroscopic approach can be neglected. Please, not that this assumption may not be valid under different flow conditions.

The second simulation is performed considering arrangement A (see Figure 1), using a 0.545m long vegetation field. A 0.0417m incident solitary wave height is simulated, according to the

free surface recorded at gauge 1. Figure 3 shows the comparison between the numerical and experimental results for two free surface gauges located offshore and onshore the vegetation field (G1 and G5 in Figure 1 for the 0.545m-long field). An additional simulation is carried out considering a lower vegetation density (arrangement B) and a longer vegetation field (l = 1.090m). Again results for the free surface gauges offshore and onshore of the meadow (G1 and G5) are presented in Figure 4 for an incident wave height equal to 0.03m. Drag coefficient is set searching for the best fitting between numerical and laboratory data. The obtained drag coefficient corresponds to 2.45 for arrangement A and 1.45 for arrangement B. These values are in agreement with the ones obtained by Huang et al. (2011), as is shown in Table 1, following a numerical approach based on Boussinesq equations.

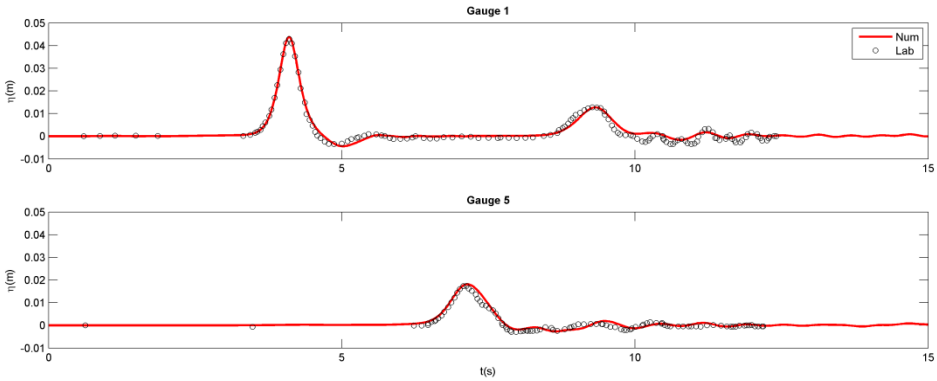

Figure 3. Free surface elevations for arrangement A and cylinder field length 0.545m and an incident wave height of 0.0417m.

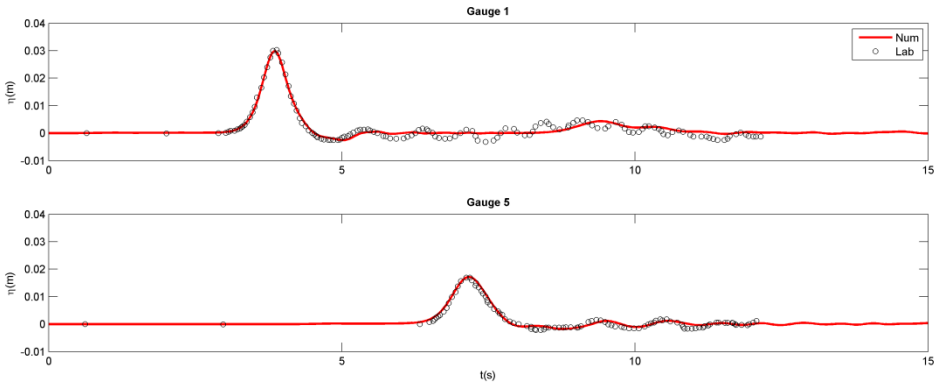

Figure 4. Free surface elevations for arrangement B and cylinder field length 1.090m and an incident wave height of 0.03m.

As can be observed in Figures 3 and 4 the model is able to reproduce the solitary wave attenuation produced by vegetation. Moreover, the reflected wave by the cylinder field is simulated with a high degree of accuracy, as can be clearly observed at the upper panel in Figure 3 at t= 9s. Almost a 30% of the incident wave height is reflected in this case. This effect is not so strong in Figure 4 due to a lower field density. The model does not reproduce small amplitude radiated waves by the individual cylinders, as can be observed in both upper panels in figures 3 and 4. Since geometry of the cylinders is not reproduced in this approach radiation cannot be solved numerically.

Arrangement	Numerical fitting	Huang et al. (2011)
A	2.45	2.45
B	1.45	1.41
C	1.52	1.52

Table 1. Comparison between obtained C_D coefficients and values given by Huang et al. (2011)

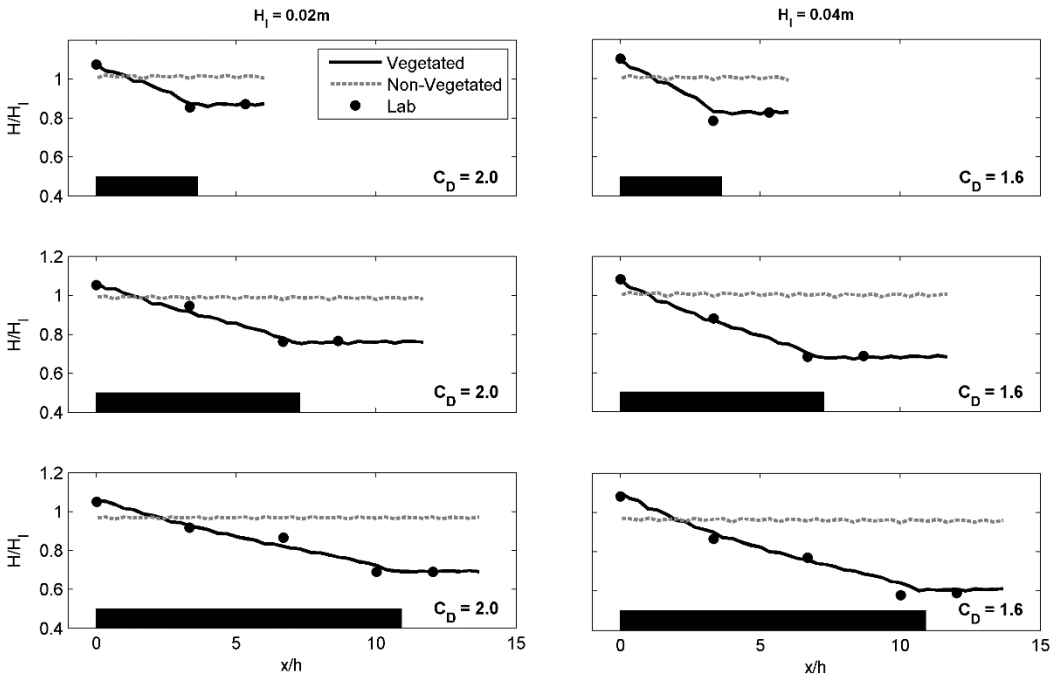

Figure 5. Wave height evolution for arrangement C and the three vegetation lengths, (0.545, 1.090 and 1.635m) and two wave heights, 0.02m (left) and 0.04m (right). Black boxes represent the cylinder field. Results without vegetation are shown in dashed line.

To extend model validation, wave height evolutions for arrangement C are compared with experimental data for three vegetation lengths, (l = 0.545, 1.090, 1.635m) and two different incident wave heights (H_i = 0.02 and 0.04m). Figure 5 shows the evolution of wave height along the numerical domain for cases with vegetation (black solid line) and without vegetation (grey dashed line). Differences point out the role played by the cylinders field in dissipating wave energy, with almost negligible wave damping in the non-vegetated cases. Best-fit drag coefficients obtained when reproducing the experiments are displayed in the figure. Wave height attenuation along the vegetation field is well reproduced by the model for all the cases.

The obtained dissipation is solely produced by drag since no breaking occurs in any of the cases considered. The drag coefficient is constant for a given wave height independently of the length of the field. For identical conditions higher waves lead to higher damping rates, obtaining up to a 40% of wave height reduction for the longest cylinder field.

3.2. Direct simulation approach

Huang et al. (2011) experiments are also used to validate the direct simulation approach using Eq. (1) and (2). In this case the N-S equations are solved considering individual rigid cylinders introduced in the domain mimicking the exact setup used in the experiments. Since the flow has to be solved between the cylinders, a finer grid is needed yielding a higher computational cost. In order to reach a balance between the computational effort and the accuracy of the results, a mesh sensitivity analysis is carried out first considering arrangement C. The analysis is focused on the numerical representation of the free surface and the solitary wave forces exerted on the cylinders according to different spatial resolutions. Figure 6 shows a zoom of the three meshes considered in the analysis.

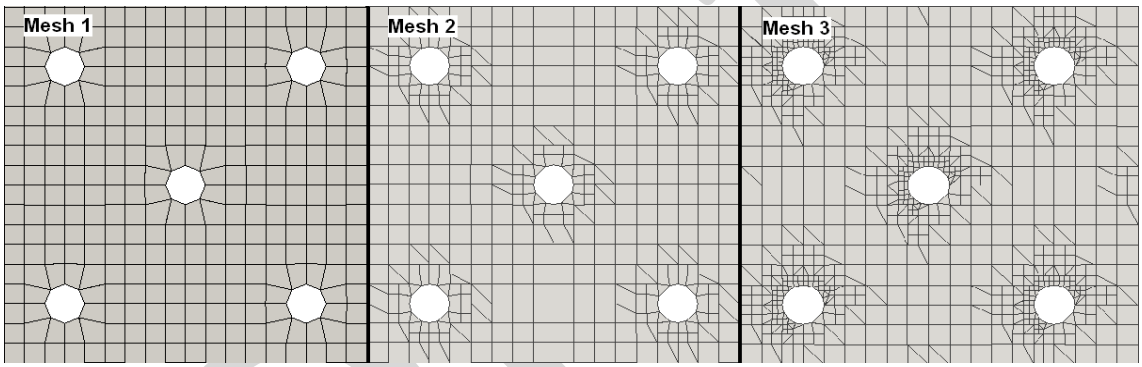

Figure 6. Mesh sensitivity analysis. Increasing resolution from left to right.

Mesh 1 corresponds to the coarser mesh and Mesh 3 is the one with the smaller cells. As can be seen in the figure, the difference between meshes lies on the refinement introduced around the cylinders in order to get a better flow representation of the small scale flow features. The three meshes share the same initial discretization, that is a uniform 0.005m in the horizontal and 0.003m in the vertical cell size. The refinement used in Mesh 2 yields to a cell size of 0.0025m in the horizontal direction and 0.0015m in the vertical. Mesh 3 has a 0.00125m cell size around the cylinders. The sensitivity analysis is carried out using arrangement C and a vegetation patch length of 0.545 m that means a total number of elements equal to 13.228.840 for Mesh 1, 14.444.400 for Mesh 2 and 18.649.780 for Mesh 3. The computational time associated to Mesh 1 is 4 days in 16 processors using a HPC machine (2.6 GHz) to simulate 10s. Computational cost for Mesh 2 and Mesh 3 is increased by a factor of 2 and 4, respectively.

Sensitivity analysis results are presented in figure 7. Wave height evolution (left panel) and the maximum forces exerted on the cylinders located along the central line of the meadow (right panel) are presented for the three meshes. Wave height is normalized by the target incident

wave height (H_I). Forces are divided by $\rho g(h+H_I)Aw$, where, ρ is the water density, g is the gravitational Aw is the cylinder wet y-sectional area ($a*(h+H_I)$).

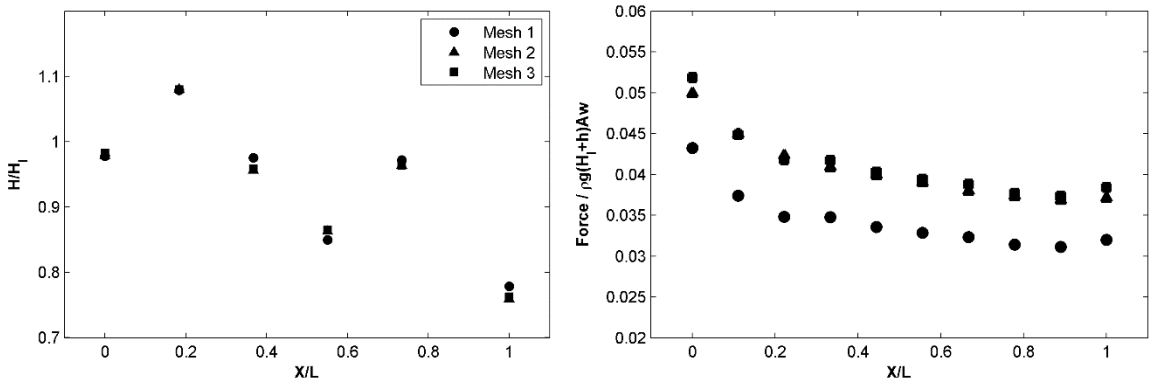

Figure 7. Comparison of wave height evolution and forces for the three different meshes. Left: Wave height evolution. Right: force exerted on the cylinders along the central line.

As can be observed in Figure 7, wave height evolution is very similar for the three meshes although higher discrepancies are found for the coarser mesh, i.e. Mesh 1. However, the differences found analysing the maximum forces exerted on the cylinders are more relevant. There is a significant discrepancy in the calculation of the maximum wave-induced forces, revealing a high resolution dependency. Mesh 1 exhibits an underestimation of the forces, due to the poor spatial resolution around the cylinders. However, no relevant differences are observed between forces calculated using Mesh 2 and 3. A maximum error smaller than 4% is found between the results obtained for the first cylinder for both meshes. In this comparison, results for the first cylinder are used because maximum forces are located there. Based on previous results Mesh 2 is selected to perform the present study.

In order to validate the numerical ability to represent the solitary wave induced flow around the individual cylinders forming the field, a simulation considering arrangement C with l = 1.635m is carried out. The κ − ω SST turbulent model is used. Numerical predictions of the free surface time history are compared with laboratory measurements presented by Huang et al. (2011) and presented in Figure 8.

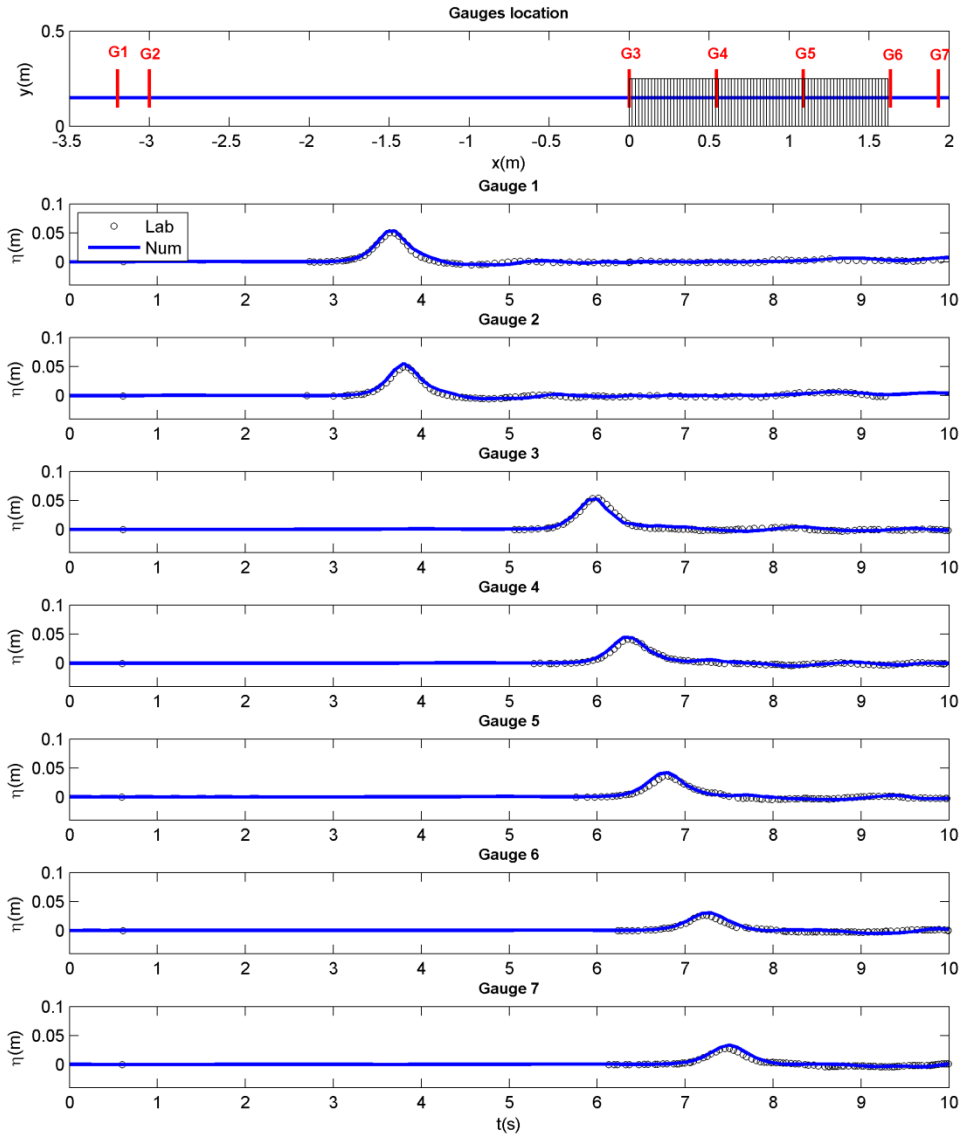

Figure 8. Comparison between numerical and laboratory free surface evolution for arrangement C and vegetation width 1.635m for an incident wave height equal to 0.05m.

Figure 8 shows a good agreement between experimental measurements and numerical results with differences in the maximum wave height smaller than 15% (gauge 7, t = 7.5s). Similar agreements have been found for all the simulated cases. Therefore, the model allows reproducing with high agreement the free surface evolution along the cylinders field considering the set of individual cylinders without the need of calibration parameters.

3.3. Comparison between both approaches

The macroscopic approach offers the advantage of a reduced computation cost. Besides the damping induced by vegetation using a drag coefficient is extensively used in combination with other wave equations. Consequently, a comparative analysis of the two-presented approaches

is carried out in this section in order to gain more knowledge about pros and cons of each approach. Numerical results are compared with laboratory experiments and shown in Figure 9.

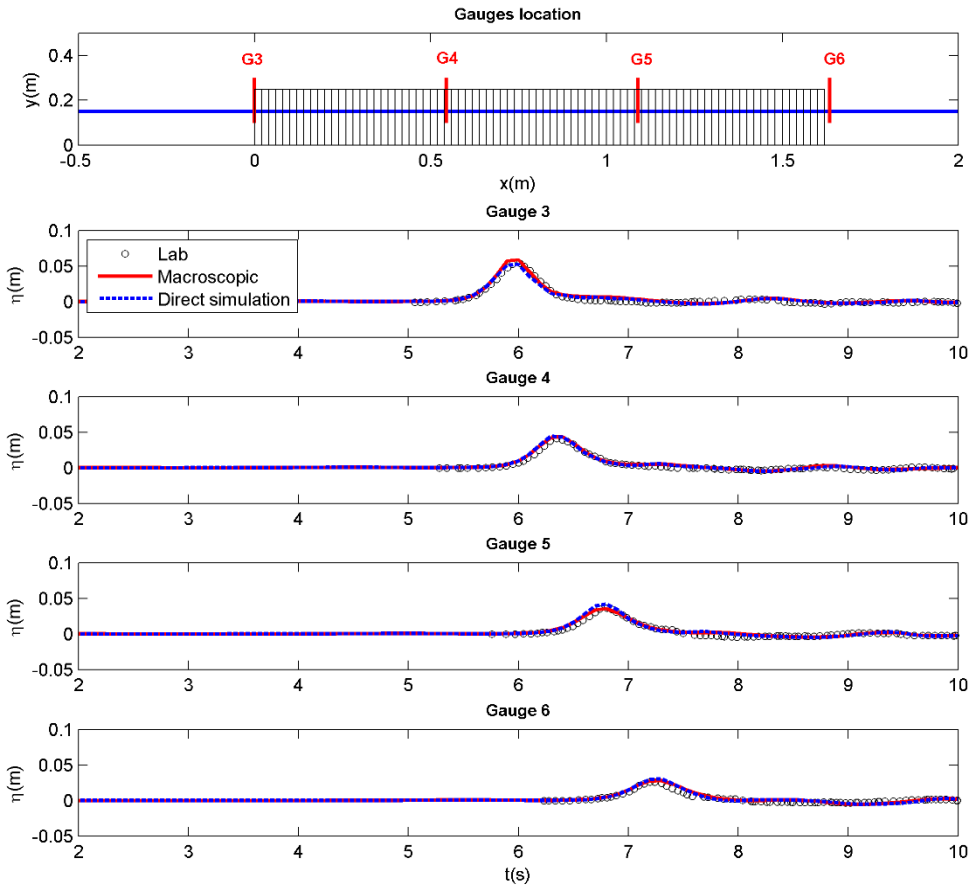

Figure 9. Free surface evolution for arrangement C and vegetation width 1.635m for an incident wave height equal to 0.05m. Numerical results considering the macroscopic approach (red solid line) and the direct simulation approach (blue dashed line) are shown.

Figure 9 shows almost no differences between the free surface results obtained with both approaches. The highest differences are found in gauges 3 and 5 where the macroscopic approach overestimates and underestimates the wave height, respectively, but differences are smaller than 10%. In gauge 3 the strong discontinuity at the beginning of the cylinders array is better reproduced when the cylinders are included in the simulations. The macroscopic approach seems not to be able to represent the edge effects at the beginning of the array so accurately. It can be seen in gauge 5 that the macroscopic flow representation produces a higher dissipation at the first half of the field. However, it can be concluded that overall, the differences between both approaches are small when modelling wave evolution along the patch.

The main difference lies on the computational cost. Mesh discretization in both approaches is very different since the introduction of each individual cylinder demands very small cells. The horizontal cell size for the macroscopic approach is 0.01m. However, this value is reduced to 0.0025m around the cylinders. This reduction at the cell size increases significantly the number

of elements of the mesh, from 1.252.496 to 19.432.400 involving a huge increase in the computational cost, from 14 hours in 4 processors to 2 days and 16 hours in 64 processors, using a HPC machine (2.6 GHz) to simulate 10s.

Despite of the increase in the computational cost, the direct numerical approach is very useful because it is free of flow parameterizations such as the ones presented in the macroscopic approach by means of the drag coefficient. It is also able to provide very useful information, not available from the macroscopic approach, such as the forces on the cylinders or detailed flow characteristics inside the vegetation patch. An example of the horizontal flow velocity and turbulent intensity ($U_I = \sqrt{2k}$, where k is the turbulent kinetic energy from the κ − ω SST model) inside the field obtained with the direct simulation is displayed in Figure 10.

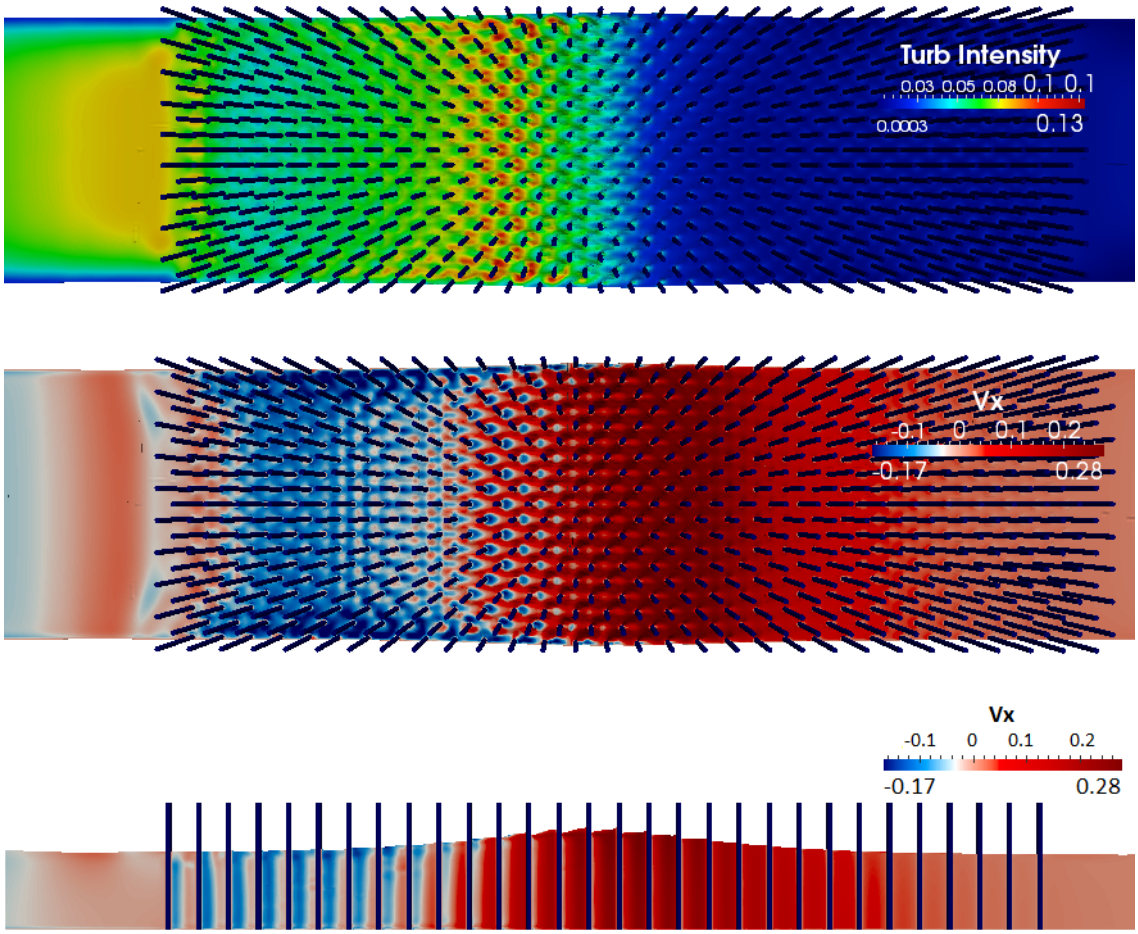

Figure 10. Turbulent intensity and horizontal flow velocity inside the cylinders field for arrangement C and wave height equal to 0.05m.

The figure shows a snapshot of the solitary wave passing along the cylinders array, when the wave crest is at the center of the field. It can be observed how flow separation around the cylinders is developed after the crest passes. According to both the horizontal velocity and the turbulent intensity fields, the shape of the wake vortices is symmetric in the middle of the numerical wave flume, as expected. However, non-symmetric vortices are visible at the lateral boundaries, which represent the laboratory flume walls. It is noticeable that the maximum

forces were obtained when the crest is reaching the cylinders, but not when the wake is developed.

4. Flow analysis based on direct simulation

Once the numerical model has been demonstrated to be able to reproduce wave induced damping with a high degree of accuracy when the geometry of the cylinders is resolved, it is used in this section to explore the detailed hydrodynamics of the flow. Simulations are performed considering the geometry of the cylinders in the numerical domain with different arrangements. This approach is free of numerical parameterizations and the drag force does not need to be parameterized. Only turbulence is modelled in the simulations by means of the $\kappa - \omega$ SST turbulent model, which uses standard coefficients.

A set of direct numerical simulations is carried out with the aim of studying the influence of several parameters on wave damping: solitary relative wave height, vegetation density and vegetation arrangement. Wave heights of H = 0.025, 0.5 and 0.15m are studied with the following associated relative wave heights H/h = 0.17, 0.33 and 0.67, respectively. Field density is taken into account by means of the use of the three densities used by Huang et al. (2011), 2228, 1108 and 560 cylinders/m2, respectively. Finally, vegetation arrangement is included in the analysis considering Huang et al. (2011) uniform arrangements (A, B and C, presented in previous section) and additional random arrangements. All simulations are run for h = 0.15 m and l = 0.545 m. Table 2 summarizes the parameters covered.

Arrangement	Wave height (m)	Relative wave height (H/h)	Distribution
A	0.025 / 0.05 / 0.10	0.17 / 0.33 / 0.67	Uniform / Random
B	0.025 / 0.05 / 0.10	0.17 / 0.33 / 0.67	Uniform / Random
C	0.025 / 0.05 / 0.10	0.17 / 0.33 / 0.67	Uniform / Random

Table 2. Relevant parameters considered in the direct numerical simulations.

The numerical domain is 4.60 m long, 0.55 m wide and 0.28 m high. A solitary wave is generated at one side of the numerical domain and active wave absorption is considered onshore allowing outgoing waves leave the domain. Mesh 2 is used following the results obtained for the sensitivity analysis presented in previous section. A sketch of the mesh discretization used for the three different arrangements (A, B and C) is shown in Figure 11including a zoom of the mesh resolution around the cylinders. The total number of volumes in the numerical mesh is 17.684.448, 15.583.200 and 14.444.400 for arrangements A, B and C, respectively.

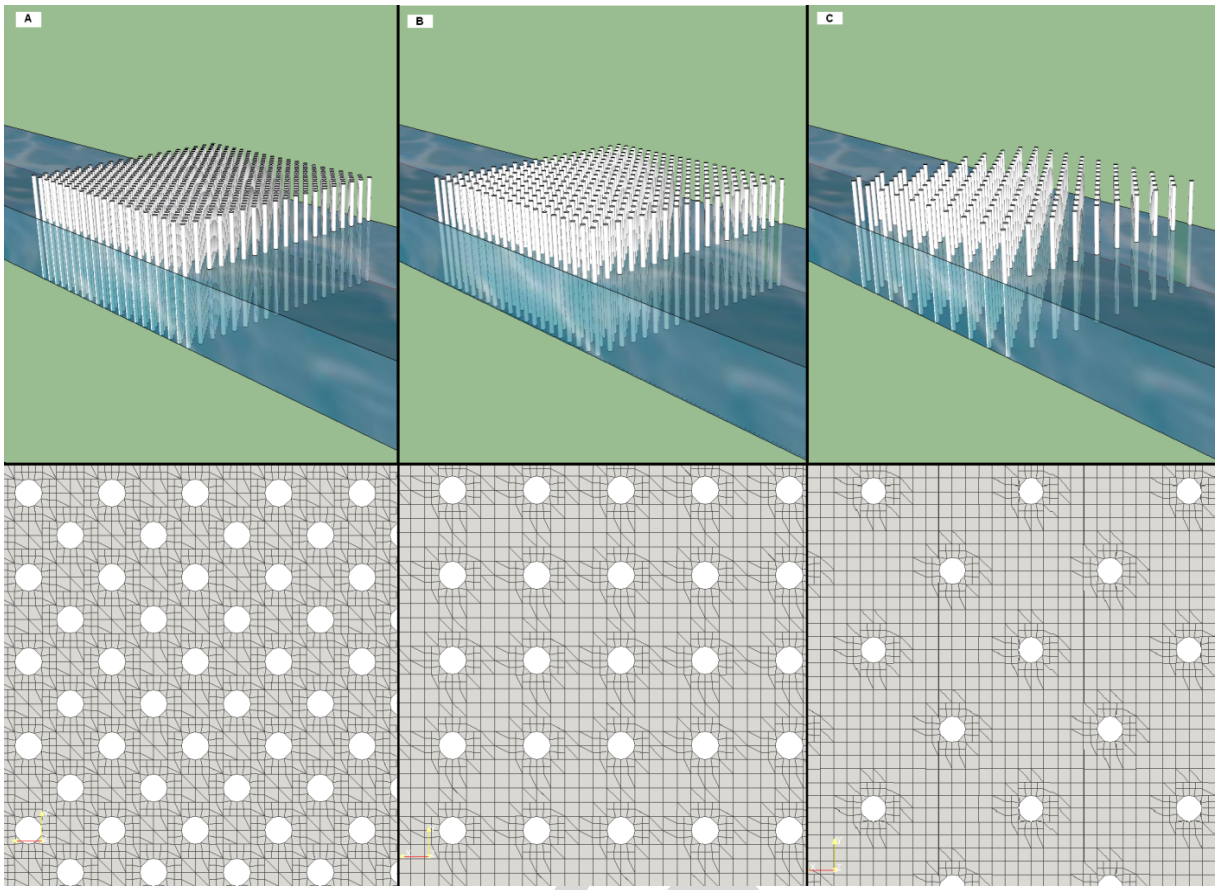

Figure 11. Cylinders introduced in the domain (first row) and top view of the considered meshes (second row) for each arrangement (A, B and C).

Free surface information is obtained from the model at different locations in order to calculate wave damping. Wave height is evaluated at three locations offshore of the meadow (X/L = -3.67, -0.92 and -0.14) and at two locations onshore (X/L = 1.10 and 1.30) for the three arrangements. Additional information is also obtained inside the meadow along the cylinders central line in all cases. Different locations are chosen depending on the arrangement. For the sake of clarity, these locations are represented in Figure 12 where the central cylinders line of the field is coloured in black. A detailed top view shows the exact location of the point, in red, where the free surface is calculated numerically. Cylinders plotted in black are the ones used to evaluate wave-induced forces, as it will be shown later.

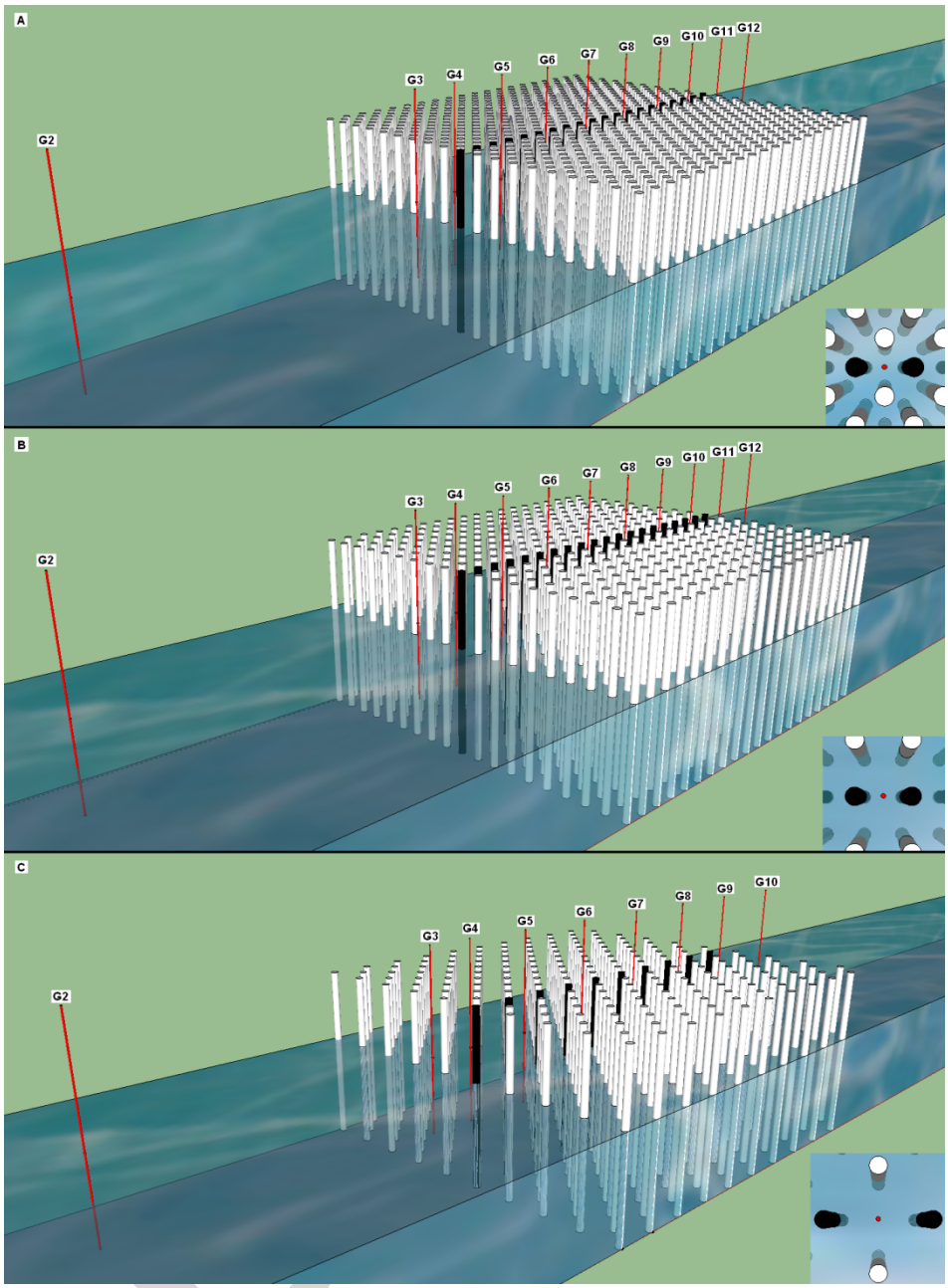

Figure 12. Gauges location (in red) for the three arrangements (A, B and C) and l = 0.545m. Top view of the location of one gauge is shown for each arrangement at the bottom right corner.

4.1. Analysis of the influence of solitary wave non-linearity

The influence of relative wave height is analysed first. The three selected wave heights (0.025, 0.5 and 0.15m) are simulated considering arrangements A, B and C with a uniform cylinder distribution. Free surface evolution along the field is studied for the different conditions. Four representative free surface gauges are selected for each arrangement, one offshore the vegetation patch (X/L = -0.92), two inside the vegetation patch (X/L = 0.30 and 0.80) and one leeward the patch (X/L = 1.30). Figure 13 shows the free surface time history at each location

for the three wave heights and the three arrangements. Free surface is normalized by the incident wave height at X/L = -0.92. Solitary waves are plotted at the same time instant to visualize changes in wave celerity when traveling along the patch.

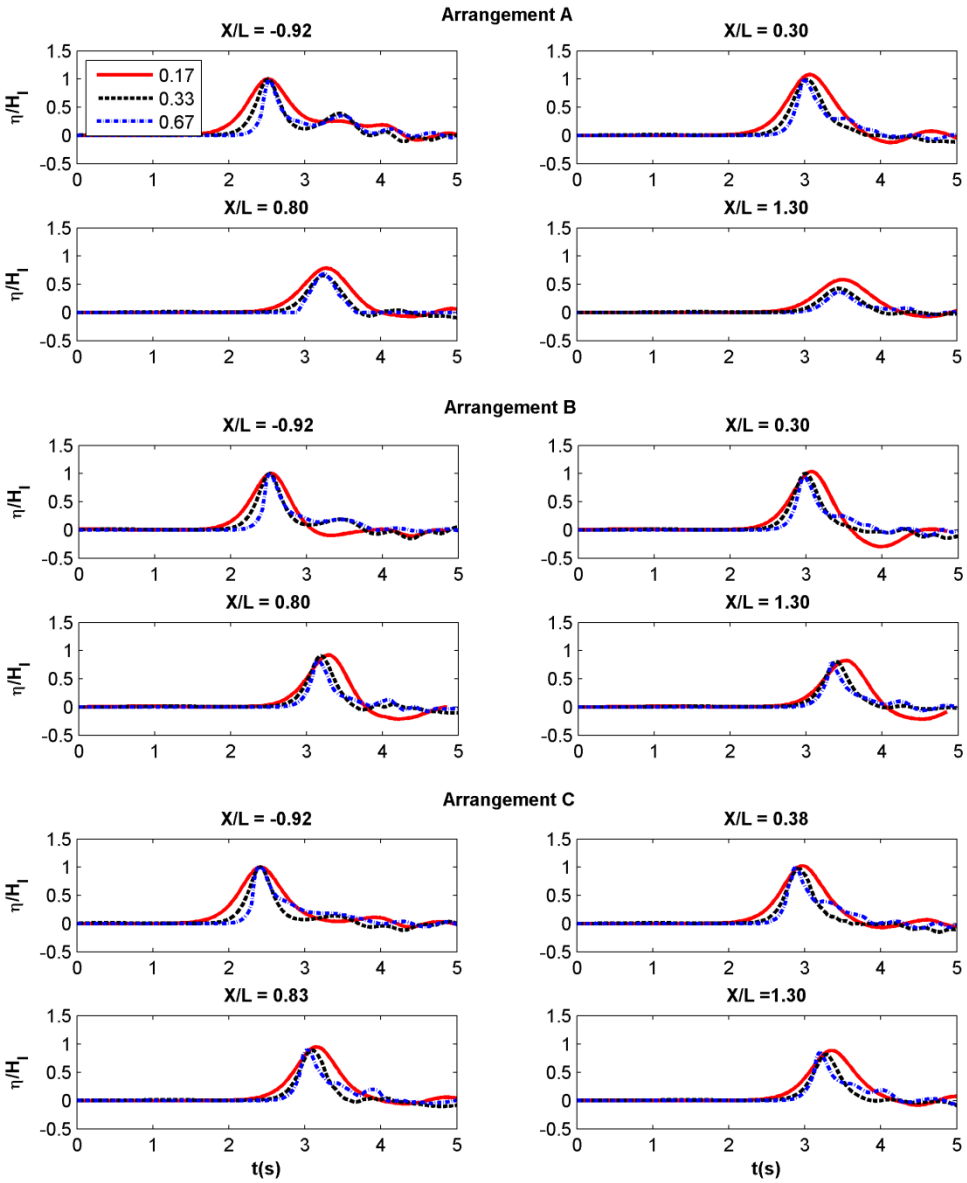

Figure 13. Free surface evolution along the cylinders field for arrangement A, B and C and H = 0.025m (red solid line), 0.05m (black dashed line) and 0.10m (blue dash-dotted line) at four locations.

The highest wave shows the largest asymmetry, with a front almost vertical and a longer tail in all the cases. Furthermore, the wave evolution along the field does not change linearly with the relative wave height. It can be observed that for the three arrangements, the smallest relative wave height (H/h = 0.17) has a different behaviour than waves with H/h = 0.33 and 0.67.

Free surface measurement in front of the field reveals a strong reflection for the densest arrangement (A) while this effect is weak for arrangements B and C. This reflection is smaller for the smallest wave and almost the same for the other two simulated waves. Free surface leeward the field shows higher wave attenuation when increasing wave nonlinearity. Although generated solitary waves travel at different speed according to their different wave height, smaller differences are found for the denser cylinders configuration (arrangement A). Momentum damping appears as an effective mechanism to reduce wave celerity and vegetation arrangement seems to play also a relevant role.

Regarding wave height evolution along the patch, the asymmetry of the highest wave is reduced for the densest arrangement where more energy is attenuated. However, for the other two arrangements, wave profile remains non symmetric along the patch, especially for the sparsest one.

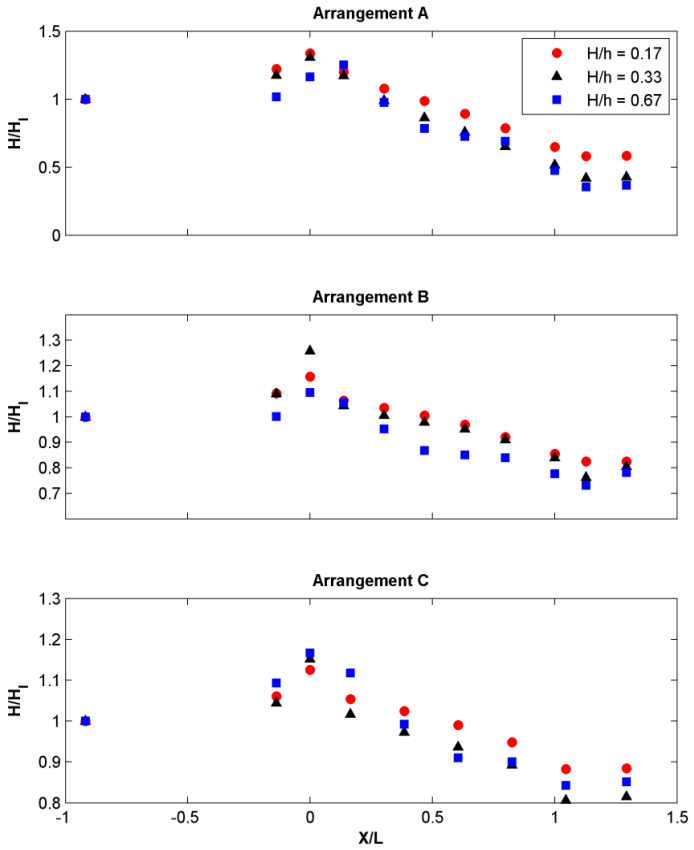

Figure 14. Wave height evolution for the three arrangements and H = 0.025m (red circle), 0.05m (black triangle) and 0.10m (blue square).

In order to evaluate wave damping produced for the three arrangements, solitary wave height evolution along the patch is presented in Figure 14. All the simulated cases present a common feature at the seaward edge of the patch: increasing wave height varying with field density. Larger values are obtained for the densest configuration (arrangement A) as a result of a local effect due to the increase of flow resistance induced by the cylinders. Wave height

enhancement factors of 1.3 are calculated in that case. Arrangements B and C show values around 1.2, as a consequence of a lower flow resistance. This effect is very relevant in the characterization of the flow behaviour at the seaward edge of the patch, as it will be discussed later. Wave height rapidly decreases with increasing relative wave height. Arrangement A shows the largest dissipation rates due to its denser configuration.

Wave induced forces at the cylinders are calculated by means of the flow and pressure fields at each individual cylinder. The central row (in black colour, in Figure 12) is chosen to be representative of the force distribution along the patch. Solitary wave induced force is obtained considering both, pressure and viscous forces on each cylinder as follow:

$$F_{max} = max\left(\int_0^{\eta}\left(p + \mu_{eff}\frac{\partial \bar{u}_i}{\partial x_i}\right)dA\right) \tag{10}$$

where η is the location of the free surface, p is the total pressure field, μ_{eff} is the efficient kinematic viscosity which includes the laminar and the turbulent contribution to shear stresses, $\bar{u}_i$ is the velocity field and *dA* the area differential along the cylinder. The maximum force exerted on the central line cylinders is obtained and represented in Figure 15 for different wave heights. The maximum forces are normalized by $\rho g(h+H_I)Aw$.

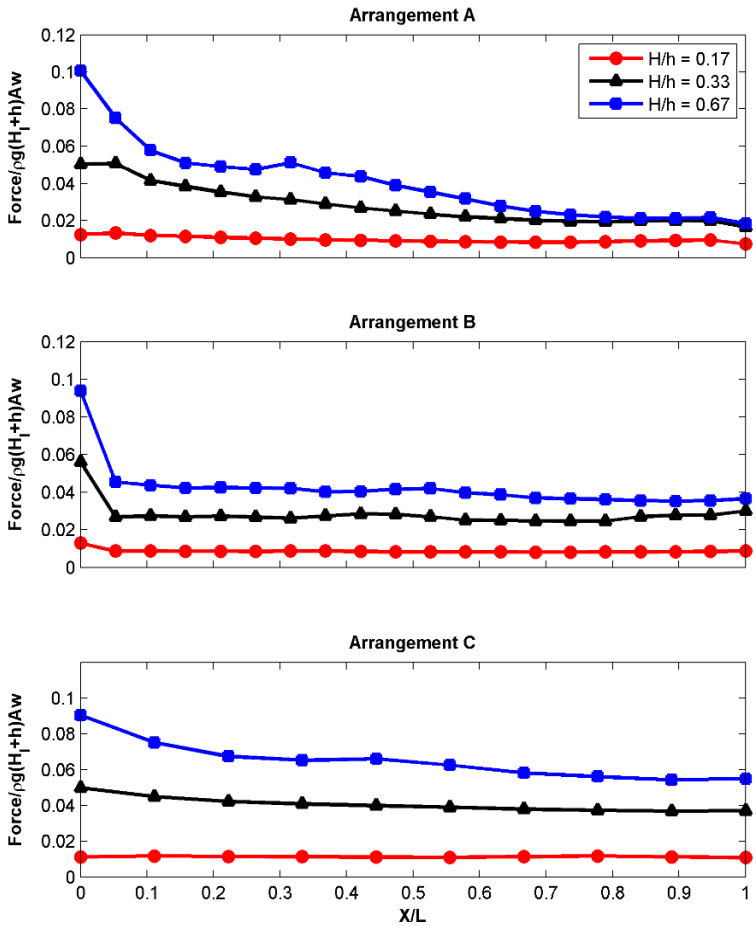

Figure 15. Forces at the cylinders of the central line for the three arrangements and H = 0.025m (red circle), 0.05m (black triangle) and 0.10m (blue square).

The wave height increase observed previously at the seaside edge induces a visible increase in the maximum force in all the cases. This feature is very relevant especially when the density of the cylinders increases, as shown for arrangement A. This effect could have a clear influence on the survival of the plants exposed to waves located at the seaside part of the field. Another important aspect derived from the results is that the maximum force increases with relative wave height if no breaking takes place. The smallest wave height shows an almost constant value of the maximum force along the three arrangements. Maximum forces slightly decrease along the patch for the other two studied wave conditions, being more relevant in the densest cylinder configuration (arrangement A). Therefore, the force reduction rate is higher for nonlinear waves.

4.2. Arrangement influence

Previous results have shown a strong dependency of the cylinder arrangement on wave evolution along the vegetation patch and wave induced forces. Characteristics such as the patch density or the cylinders arrangement are studied more in detail in this section. First, arrangements A, B and C, defined according to Huang at el. (2011) experiments, are studied to determine the influence of a regular spatial distribution on flow patterns. Due to the motivation found in real mangrove forest, which follow a random distribution in space, additional simulations are performed. Three new arrangements are designed considering the densities of the uniform arrangements, but randomly distributed. Wave damping and wave-exerted forces are analysed in all the cases.

4.2.1. Uniform distribution

Solitary wave height evolution and forces exerted on the cylinders are represented in Figure 16 for the three uniform arrangements A, B and C. The same three wave conditions used in the previous section are considered here.

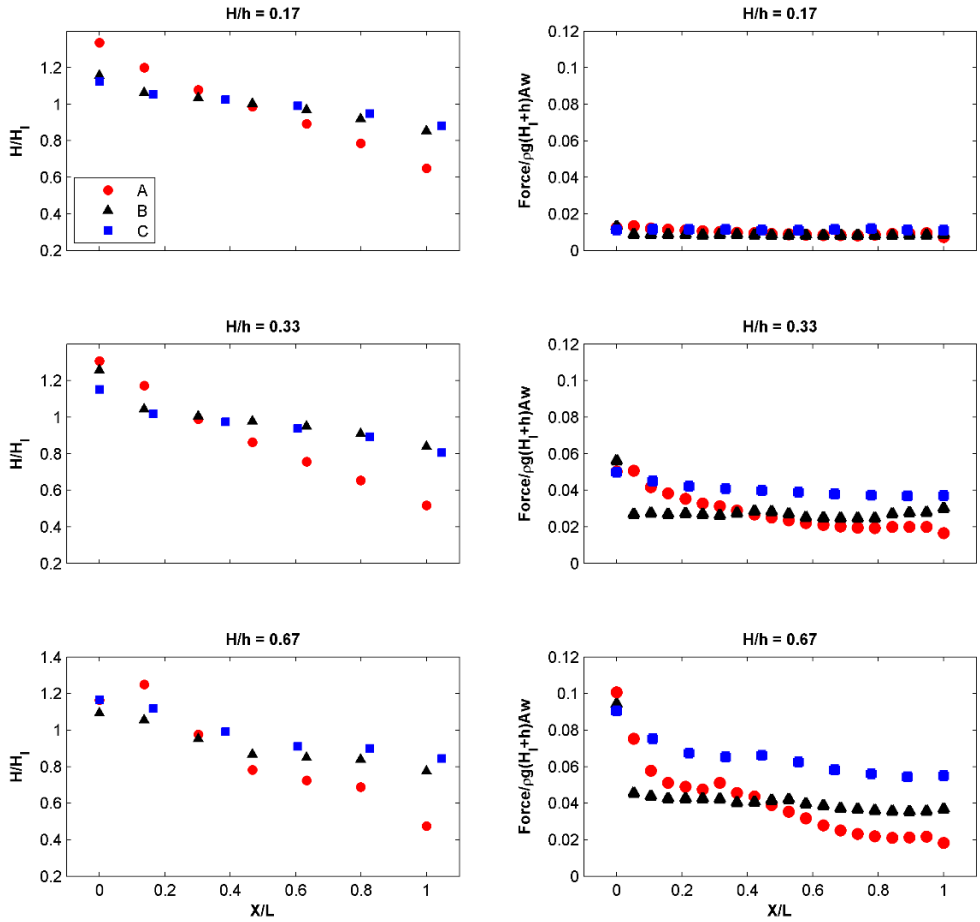

Figure 16. Wave height evolution (left column) and forces exerted on the cylinders (right column) for the three wave heights (in vertical) and the three cylinders arrangements (A, B and C).

Numerical results presented in Figure 16 show a strong dependency on the cylinders arrangement of wave height evolution. This pattern is related to the density associated to each configuration, namely N = 2228, 1108 and 560 cylinders/m^2 for arrangement A, B and C, respectively. Arrangement A, with the highest density, produces a higher flow blocking at the seaward edge of the patch yielding a higher increase in wave height. Wave attenuation appears stronger for the denser arrangement at inner locations in the patch showing the highest wave attenuation at the end (X/L=1). A similar behaviour for solitary wave evolution along the field is found for arrangement B and C. That feature is due to the low density in arrangement C and the existence of preference flow channels in arrangement B, as it will be discussed later, which makes the flow through the field easier, developing low dissipation rates.

Figure 16 also shows the strong influence of plant arrangement on the maximum force acting on the cylinders. Arrangements A and C follow a five cylinder stencil configuration whereas arrangement B considers cylinders forming a uniform square grid. As can be observed, the maximum force on the first cylinder is almost the same for all arrangements, as expected. The first row of cylinders is directly exposed to wave action. However, force evolution differs along the field for each arrangement. A rapid and large reduction in the maximum force is observed

for arrangement A, showing the lowest force values at the end of the patch. Cylinders damp most of the wave energy due to the higher density and the smaller spacing between cylinders. Therefore, this densest arrangement produces the highest reduction of forces acting on the cylinders in accordance to the wave height damping. Maximum force is less attenuated in arrangement C due to the low density and the larger spacing between cylinders. Finally, arrangement B shows a different behaviour with an almost constant maximum force along the patch, except for the first cylinder. The uniform squared configuration produces clearly different preference flow channels due to the large spacing between cylinders. Flow is developed along the gaps, which are oriented in the wave propagation direction. This effect can be seen in figure 17, which presents a top view of three snapshots of the horizontal velocity field magnitude at the free surface for the three arrangements. As can be seen for arrangement B (middle row), wave induced flow is channelled along the oriented uniform gaps as the solitary wave is passing along the field. Cylinders are not directly exposed to flow and they are shadowing each other. For that reason almost constant maximum forces along the vegetation are found. This effect is not seen for arrangement A, with a higher density, smaller cylinders spacing and non-staggered configuration. Although arrangement C also corresponds to a non-staggered configuration, the large cylinders spacing produce the existence of clear developed preference flow channels.

It is also interesting to note the change in wave celerity seen for the three arrangements. Free surface elevation snapshots at time step 6.2 s show that the wave crest is located at different positions for the three arrangements. The higher the density of the field the higher the celerity reduction. For the same time step the wave reflected from the meadow can be observed. Reflection is also directly related to the cylinders density.

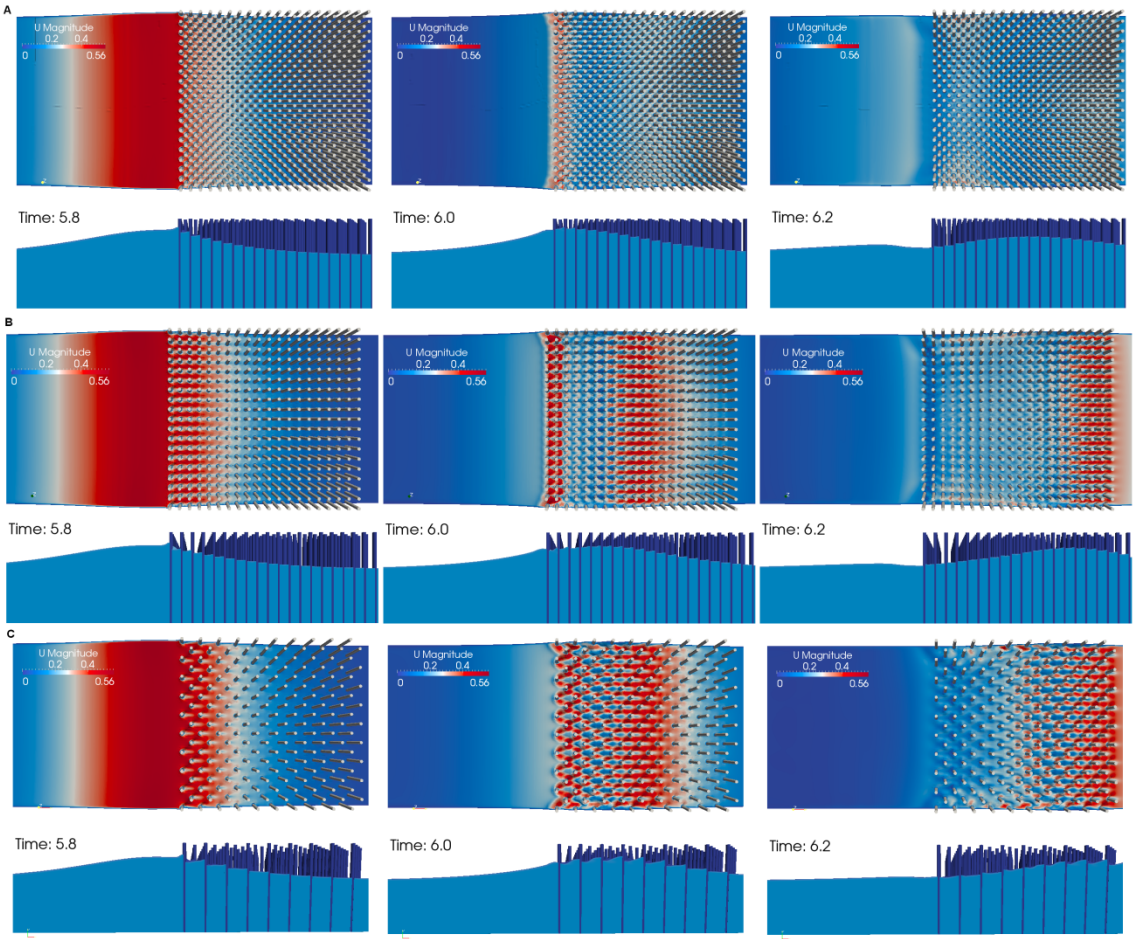

Figure 17. Flow velocity and free surface elevation for three time steps in the three arrangements A (upper row), B (middle row) and C (lower row).

As a conclusion, it is noted that the wave induced forces and the wave attenuation due to the rigid vegetation is clearly influenced by the cylinders arrangement. Wave damping rates are sensitive to relative location, density and spacing between cylinders. Flow patterns developed under arrangement B perhaps do not represent realistic scenarios found in nature and could lead to wrong conclusions due to a very uniform and unrealistic arrangement.

4.2.2. Random distribution

Although the influence of random vegetation distribution in flow patterns under uniform currents has been investigated (i.e.: Koch and Ladd, 1997; Nepf, 1999; Tanino and Nepf, 2009), only few studies have considered wave flow (e.g.: Anderson, 2010). In order to overcome the limitations found for a uniform arrangement and to study more realistic configurations, three new simulations are performed considering a random distribution of cylinders.

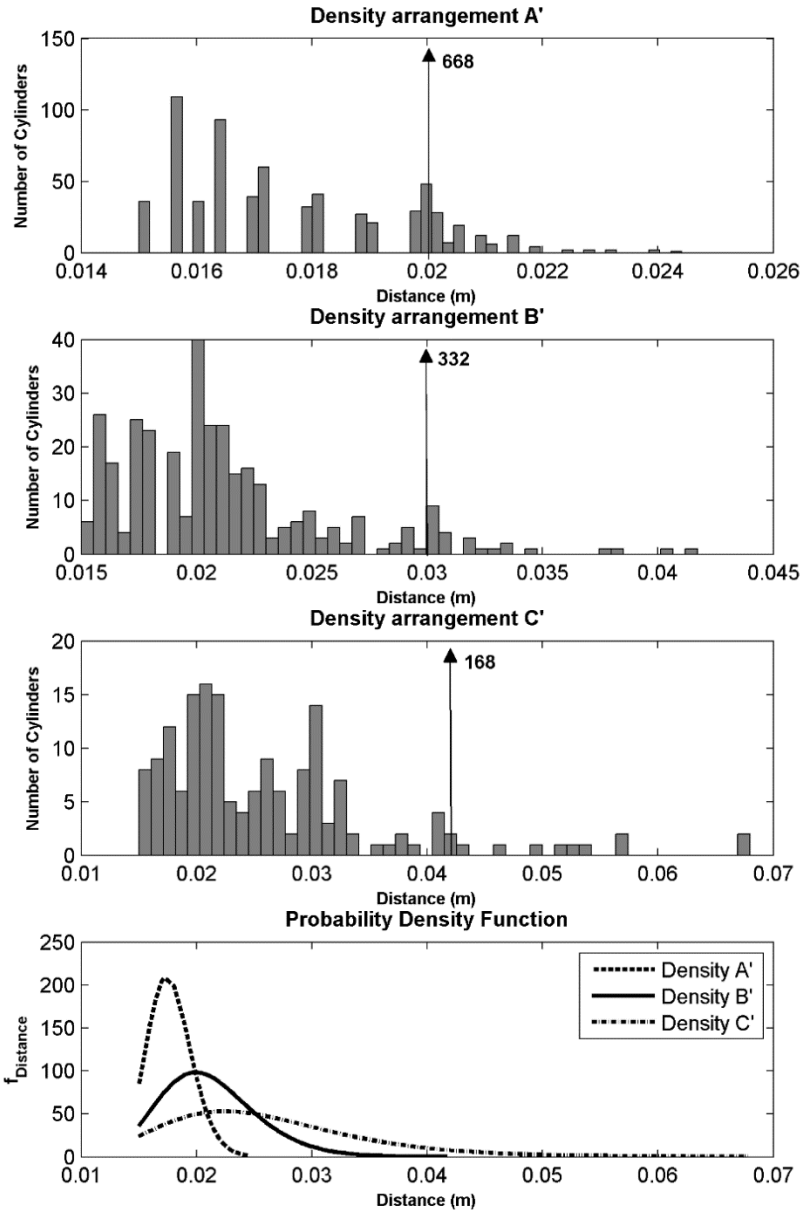

Figure 18. Cylinders distance histogram for densities of arrangements A', B' and C'. Arrows represent the values for uniform arrangements. Last image shows the probability density function for the three random configurations.

New configurations (A', B' and C') are calculated considering the cylinders density for arrangements A, B and C (N = 2228, 1108, 560cylinders/m^2, respectively) for the same vegetation patch length, i.e.: 0.545m. In order to obtain random distributions, the total number of cylinders associated with each density is disposed randomly, with a minimum distance between cylinders, equal to half of the cylinder diameter. Figure 18 shows the cylinders spacing histogram associated to each density. The total number of cylinders for each uniform arrangement is included in the figure. The corresponding distance of uniform

distributions is presented in each panel by means of an arrow. The lower panel shows the cylinders spacing lognormal probability density function for each random configuration.

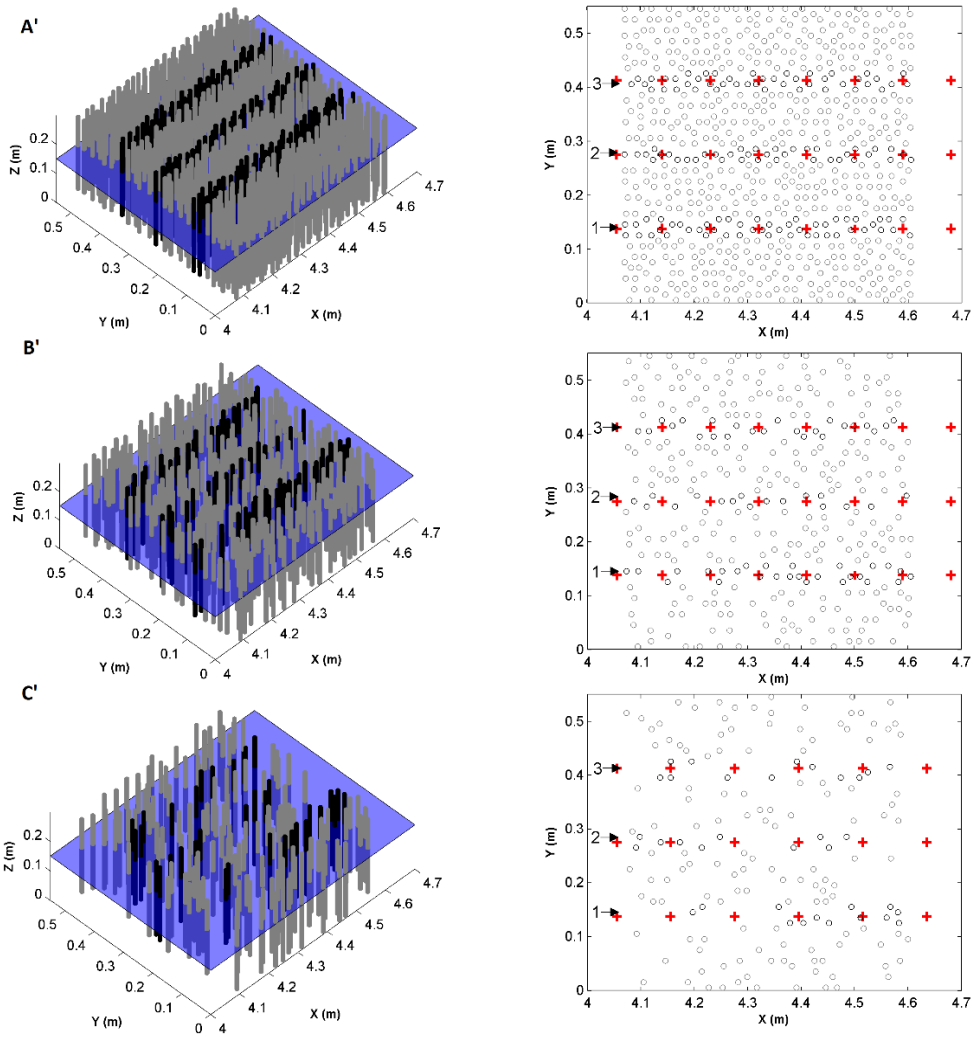

Figure 19. Random cylinders distributions for density of arrangements A', B' and C'. Black cylinders are located in the three control sections.

Figure 19 shows the three configurations used in this study for the cylinders random distributions. A top view is shown at the right panels for each arrangement. In order to study wave height evolution and the forces exerted on the cylinders, three longitudinal transects along the field, shown in the figure, are considered in order to get representative results. Relative wave height is evaluated at the same locations as the ones used for the uniform arrangements, represented with red crosses in figure 19. Forces are evaluated in the cylinders plotted in black in the three panels.

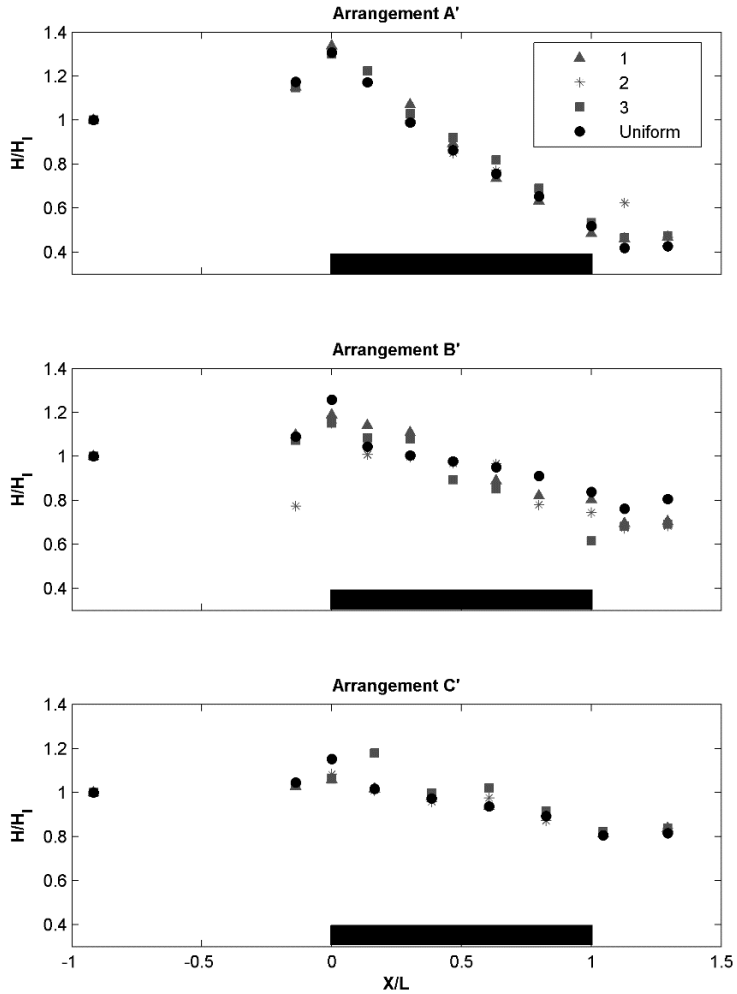

Figure 20. Relative wave height evolution along the cylinder field for random and uniform arrangements A', B' and C'. Results for control sections 1 (triangles), 2 (stars) and 3 (squares) are represented for random configurations.

Figure 20 shows wave height evolution along the vegetation patch for the three random arrangements, along the three transects shown in Figure 19. Results corresponding to the uniform configuration are also included in the plots. As can be observed in the figure, wave height evolution is very similar for random control sections and uniform arrangements. The highest differences are found for arrangement B' where wave damping produced for the random distributions is larger than the one obtained for the uniform patch, revealing the strong influence of the preference channels in the flow pattern. Additionally some local effects can also be observed from the numerical results. Wave height increase at the seaward edge of the patch is almost negligible for arrangement C' (lower panel) probably due to the fact that the number of cylinders at the beginning of the field is lower in the random configuration. The wave increase effect is located farther inside the field for results in transect 3.

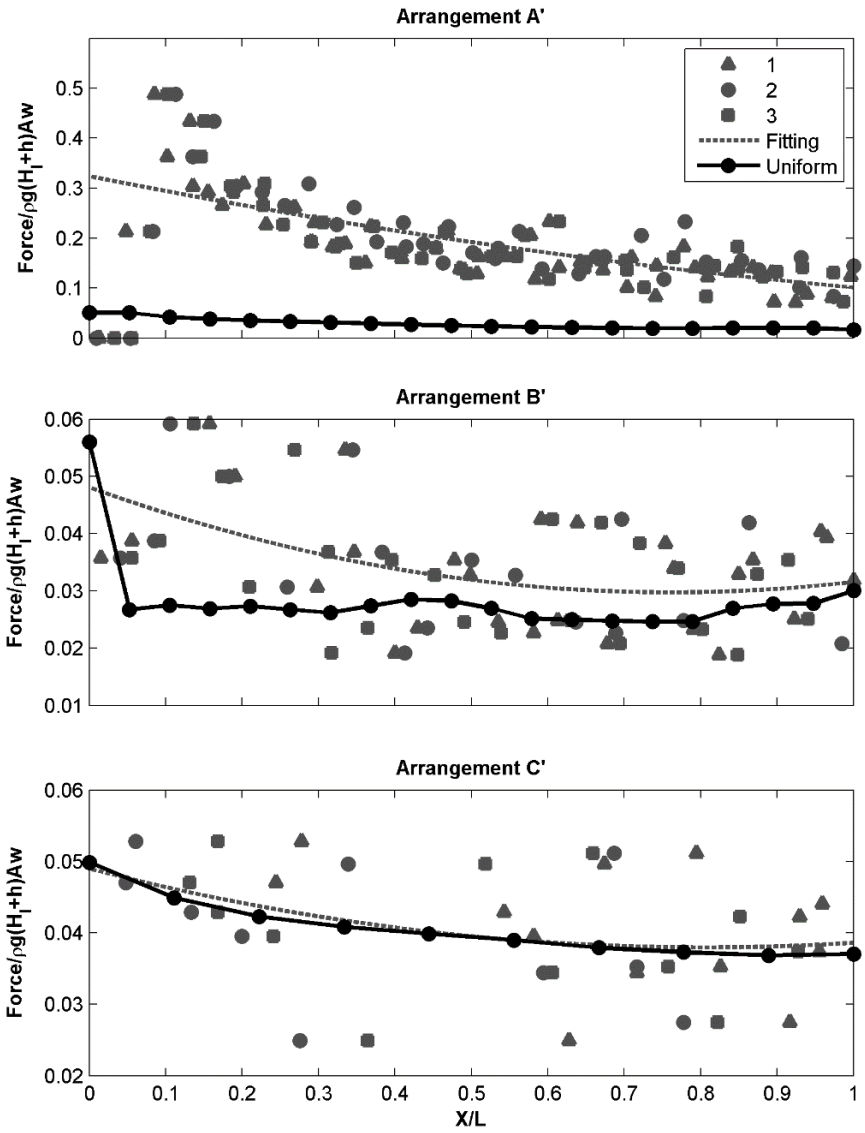

Figure 21. Forces exerted on the cylinders of the three control sections of the random configuration and the cylinders of the central line of the uniform distribution.

Consequently, in terms of wave damping and neglecting very local effects, overall density, field length and relative water depth are more relevant than plants distribution within the field. Differences increase with decreasing plants distribution but for cases considered, they remain in a ±10 - 20% of the uniform distribution damping results. It can be concluded that based on these results dynamics triggered by wave height differences are only anticipated at the edges of the field.

Forces are calculated according to Eq. (10). The evolutions of the maximum forces along the patch are plotted in Figure 21. Results correspond to cylinders included in the three transects. They are plotted together with a quadratic fitting law in order to estimate averaged values along the patch. Results obtained for uniform distributions are also included in the plot. One common aspect observed in the figure is the large dispersion of the maximum force obtained for the random arrangements. This is mostly due to local effects in the velocity flow field linked to the relative location of the cylinders. However, a decaying trend is observed in the

maximum force along the patch in the individual force values, also confirmed by the fitting curve. Another important aspect obtained from the simulations is that for the uniform arrangement the maximum force is lower along the patch. Random distributions turn in decreasing stems alignment and increasing grouping. This lowers the probability of wake sheltering on individual downstream cylinders. This effect is higher for larger density values. Thus, for the densest arrangement the force obtained with a uniform configuration is less than half the one estimated for the random case. The shadowing effect between cylinders is less effective in a random distribution, increasing the wave-exerted force. This feature is also visible when wave induced flow is analysed.

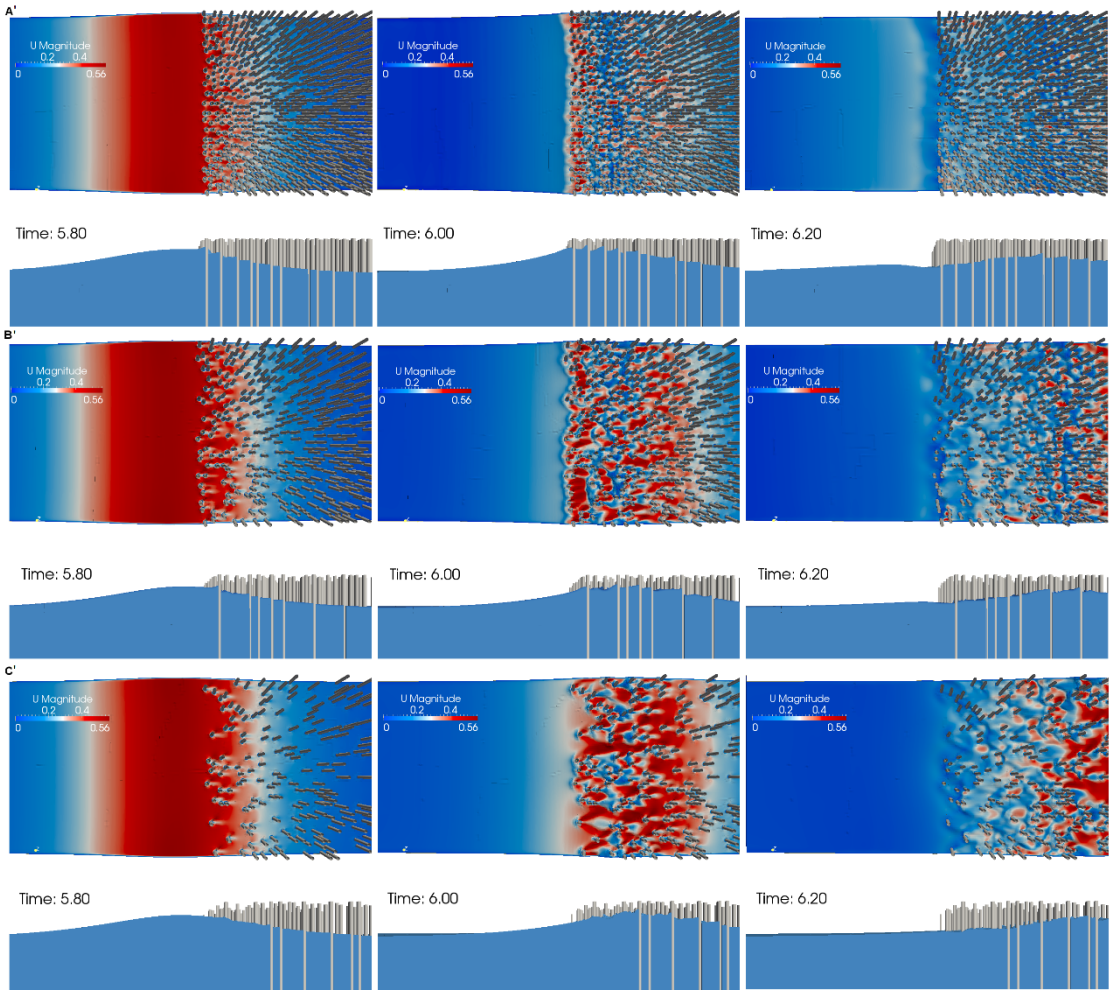

Figure 22. Flow velocity and free surface elevation for three time steps in the three random arrangements.

Figure 22 shows snapshots of the horizontal velocity fields at the free surface developed between the cylinders for the three random configurations. Three different time steps are presented when the solitary wave is travelling along the field. A side view of the free surface is also plotted in the lower panels. Results show irregular flow patterns in comparison to the regular velocity fields observed for uniform cylinder arrangement (Figure 17). Both wakes, created behind the cylinders, and flow accelerations, formed at the constrictions by the random paths created around the cylinders, are clearly observed. Moreover, isolated cylinders

can be observed in the less dense configurations (two lower panels) as a result of the random arrangements, responsible for the larger forces induced by waves.

As a summary, it is very important to point out that the idealized arrangements that are usually tested in laboratory experiments or simulated numerically give reasonable good results in terms of overall wave damping. However, large differences are found in the forces exerted on the vegetation for uniform and random distributions. Generalizations obtained from uniform arrangements could lead to underestimation of wave-exerted forces, especially for high dense configurations and the ones that could be found in nature, which follow random arrangements.

4.3. Discussion on the numerical approach

So far, it has been demonstrated that both numerical approaches provide an accurate wave height evolution along the cylinders array but with different computational costs. Regarding the estimation of the forces exerted on the individual elements, the first approach allows obtaining these forces directly since individual cylinders are introduced in the domain. However, the evaluation of forces using the macro-scale approach is only possible considering the drag force formulation presented in Eq. (6).

In this section the differences between the two approaches in force calculation is examined. Drag coefficients obtained in the model validation in Section 3 are used to calculate maximum forces on the cylinders for the macroscopic approach. The characteristics of these cases as well as the calibrated drag coefficient for each case are specified in Table 3. The Reynolds number associated to each wave condition is also shown in the table. This number is defined as $Re = \frac{aV_c}{\upsilon}$, where a is the cylinder diameter, V_c the maximum solitary wave celerity ($\sqrt{g(h+H_i)}$) and υ the dynamic viscosity.

Run	Arrangement	Width (m)	H_i (m)	Re	C_D
V1	A	0.545	0.041	13.688	2.45
V2	B	1.090	0.03	13.288	1.45
V3	C	1.635	0.05	14.007	1.52

Table 3. Validated cases characteristics and calibrated drag coefficients

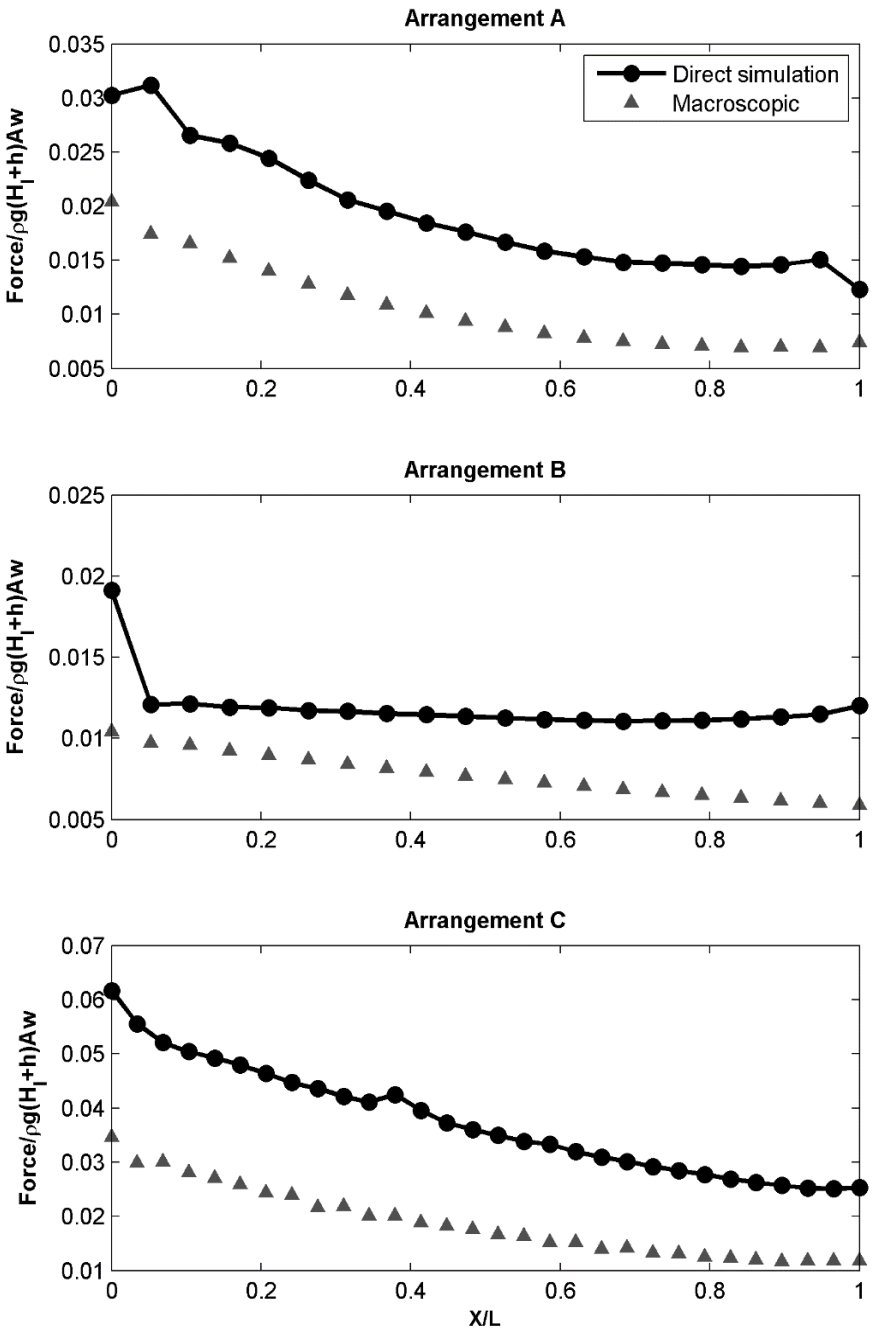

Figure 23. Forces on the cylinders of the central line (black dots) and at those locations for the drag approach (grey triangles).

Maximum forces on the cylinders are presented in figure 23 for the three uniform arrangements.

Although the velocity field obtained with the macroscopic approach is not representing a real velocity field inside the cylinder array, it was demonstrated by Maza et al. (2013) that a very accurate reproduction of the flow inside the vegetation is achieved. In that study, ADV measurements obtained inside a flexible vegetation patch were compared with numerical results obtained using the same approach showing a high degree of agreement. Following the same procedure used in experimental analysis (i.e.: Mazda et al, 1997, Strusinska-Correia et al.,

2013), wave forces are characterized here using the velocity field. Figure 23 shows a clear mismatch between values from both approaches. Maximum force is underestimated if using the macroscopic modelling. The trend observed for the force is the same for both approaches, decreasing along the patch. Results for arrangement B do not obey to that trend in the direct simulation pointing out again the influence of the flow patterns along the preference flow channels created along the direction of wave propagation. The macroscopic approach is not able to catch this feature and keeps a monotonic damping along the field.

In order to study more in detail the differences found between both approaches a new set of simulations is performed. The numerical model is used as a numerical laboratory, and the simulations, which consider the individual cylinders, are used as a reference to determine the drag coefficient value for the macroscopic approach. Nine simulations are performed considering arrangements A, B and C and three wave heights (0.025, 0.05 and 0.10m). The drag coefficient for each simulation is set to obtain the same wave damping as in the simulations run considering the individual cylinders. Following this procedure, the obtained drag coefficient values as well as the run characteristics are shown in Table 4.

Run	Arrangement	Width (m)	H_i (m)	Re	C_D
1	A	0.545	0.025	13.102	3.45
2	A	0.545	0.05	14.007	2.35
3	A	0.545	0.10	15.660	1.55
4	B	0.545	0.025	13.102	1.5
5	B	0.545	0.05	14.007	0.7
6	B	0.545	0.10	15.660	0.6
7	C	0.545	0.025	13.102	2
8	C	0.545	0.05	14.007	1.52
9	C	0.545	0.10	15.660	1

Table 4. Calibrated drag coefficient

The obtained drag coefficients vary consistently with wave height and Re. The wave height evolution obtained with these drag coefficients is compared with the results obtained with the direct simulation approach for the uniform arrangements in Figure 24.

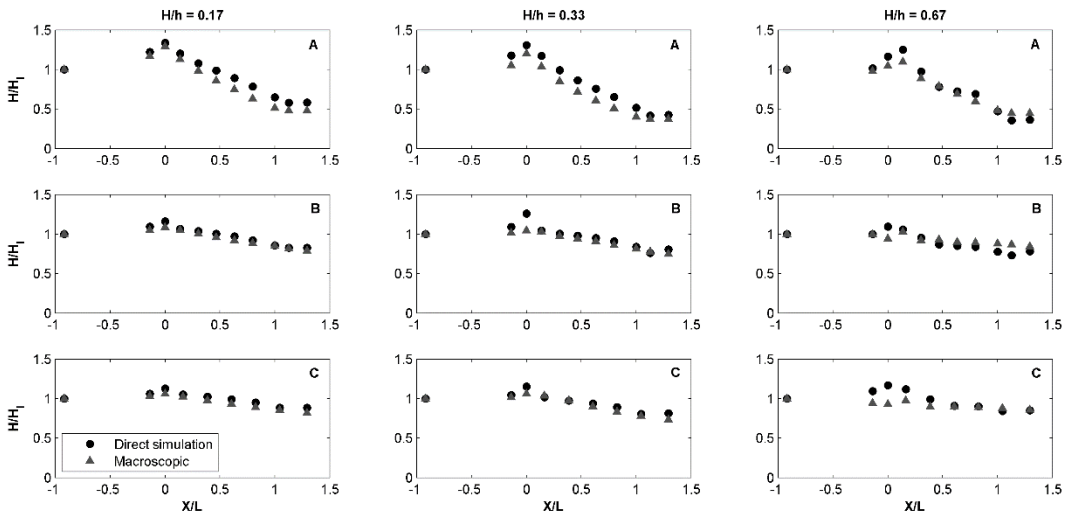

Figure 24. Wave height evolution comparison between both approaches.

As can be observed in Figure 24, wave height evolution is very well reproduced by the macroscopic approach. Minor discrepancies are observed at the edges of the meadow where the local effects produced in the cylinders field are not reproduced precisely using the macroscopic approach, especially for arrangement B. Therefore, although there is a good agreement between both approaches attending to the general wave height evolution, the local effects at the edge are not captured so well. These effects are more important when the nonlinearity of the wave increases as can be observed for cases with H/h = 0.33 and 0.67.

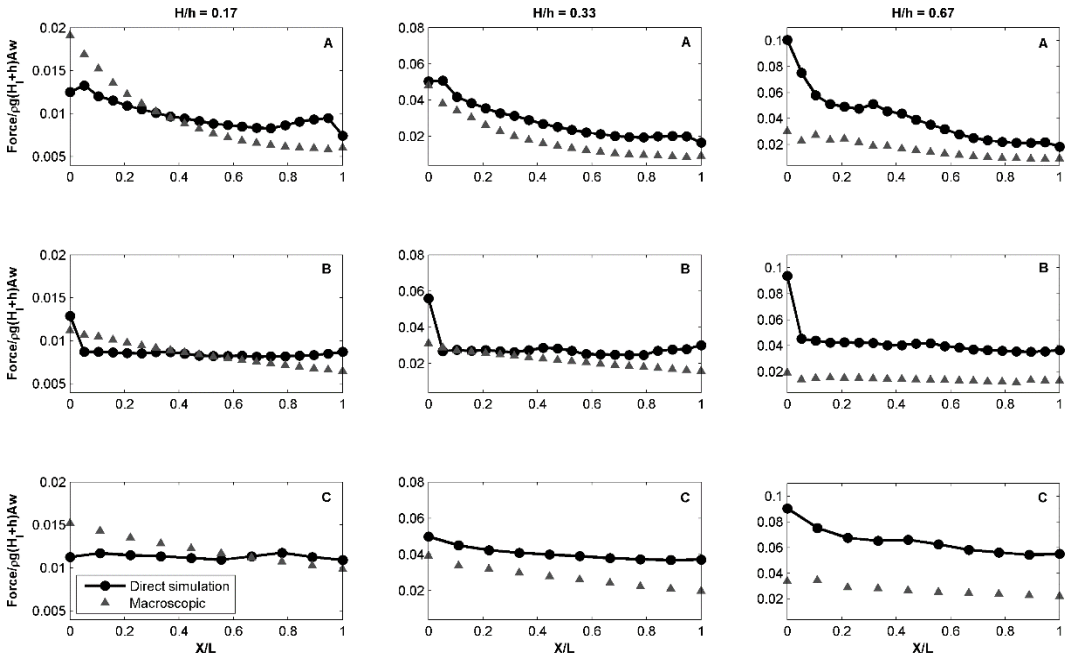

Figure 25. Forces at the cylinders of the central line (black dots) and at those locations for the drag approach (grey triangles) for the nine simulations considering the three arrangements and three different wave heights.

The drag force associated to these new simulations is also evaluated. Figure 25 shows the comparison between both approaches. Important discrepancies are obtained when forces are estimated using both approaches, not only in the values but also in the trend followed by the force along the patch. It can be observed that for the cases with the smallest wave height there is a force overestimation around the first half of the meadow that turns into an underestimation in the second half for the three arrangements for the macroscopic approach. This effect is higher for the arrangements with higher density. However, when the wave nonlinearity increases, forces obtained with the drag approach are smaller than the ones recorded simulating the individual elements. This effect is stronger if the wave nonlinearity increases. The forces obtained with the macroscopic approach for the location of the first cylinder are three times smaller than the ones recorded simulating the individual elements. Therefore, maximum forces obtained from the macroscopic approach are underestimated significantly for higher nonlinear waves.

The weakest point of the use of the macroscopic approach is the determination of the drag coefficient which has been varied according to the flow characteristics and cannot be predicted beforehand. Although several formulations can be found in the literature to estimate the drag coefficient for waves damped by vegetation (e.g.: Mendez et al., 1999; Maza et al., 2013) and more recently, waves and current attenuation (Hu et al., 2014), none of them are especially fitted for solitary waves. Tanino and Nepf (2008) proposed an empirical formulation for the mean drag coefficient for random cylinders arrays:

$$C_D = 2\left(\frac{\alpha_0}{Re} + \alpha_1\right) \tag{11}$$

where α_0 and α_1 are two empirical parameters that depend on the solid volume fraction (ϕ = volume of cylinders/total volume): $\alpha_1 = (0.46 \pm 0.11) + (3.8 \pm 0.5)\phi$ and $0 \leq \alpha_0 \leq 0.85$. The formulation for unidirectional flow and emerged vegetation presented by Cheng and Nguyen (2011) is also considered:

$$C_D = \frac{50}{Rv^{0.43}} + 0.7\left[1 - exp\left(-\frac{Rv}{15000}\right)\right] \tag{12}$$

where $Rv = \frac{r_v V_c}{\nu}$ with $r_v = \frac{\pi}{4}\frac{1-\lambda}{\lambda}a$ and λ is the fraction of cylinder-occupied bed area. The drag coefficients obtained from the best fitting are plotted in figure 26 and compared with existing formulas as a function of the Reynolds number. In this paper, V_c has been defined as the maximum solitary wave celerity. The three arrangements are presented separately to better compare with both formulations.

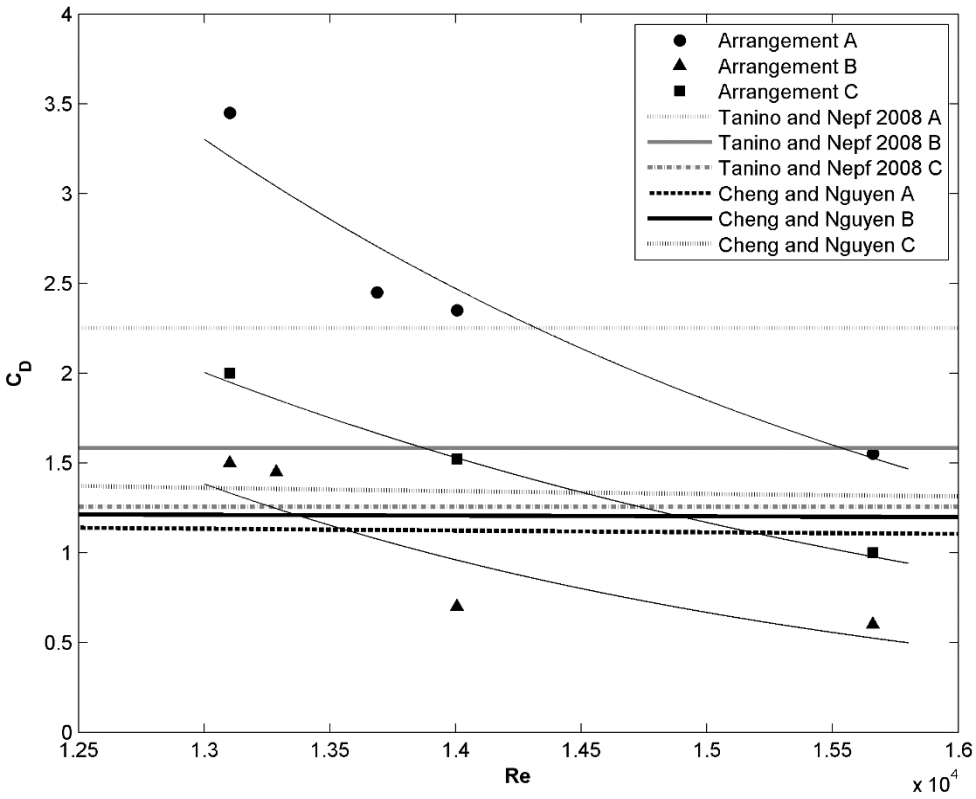

Figure 26. Calibrated drag coefficients and formulas from literature.

As can be observed existing formulations do not correspond with the calibrated drag coefficients obtained numerically. Neither the formula presented by Tanino and Nepf (2008) nor the one proposed by Cheng and Nguyen (2011) are able to capture the change produced in the drag coefficient for the simulated Reynolds number range. Therefore, it seems necessary to perform new studies to obtain an appropriate formulation for this type of conditions where the hydrodynamic forcing is a solitary wave and the rigid elements are emerged. Also the meadow characteristics should be included. Fittings obtained for the different arrangements shown in Figure 26 reveal clear differences in the values of C_D for the same Re depending on the arrangement, revealing the important role played by the vegetation density on the drag coefficient. Furthermore, it is interesting to note that drag coefficient values for arrangement B are smaller than the ones obtained for arrangement C which has a small density. This is due to the cylinders arrangement and the preferable flow channels produced in arrangement B, perhaps not representative of a real mangrove forest.

5. Conclusions

The numerical modelling of the interaction of tsunami waves with mangrove forests is addressed in this study as a first approach by means of solitary waves impinging on emergent rigid cylinders. Two different numerical approaches are followed: a direct simulation of the

flow field considering the actual geometry of the cylinders array and a macroscopic modelling of the flow within the forest, which introduces a drag force to model the momentum damping created by the plants.

To our knowledge, this is the first time that a three-dimensional model is presented to model wave damping by vegetation including an adapted turbulence model for macroscopic flow modelling around vegetation. The model is validated for both approaches using laboratory data with a very good agreement with laboratory measurements for free surface evolution along the mangrove forest. While macroscopic modelling needs the calibration of the drag coefficient, direct simulation approach is free of parameterizations. Direct simulation has proven to have a high potential to be used to study local effects and more realistic scenarios. The main drawback brings the high computational cost.

The model is used as a numerical laboratory to get very valuable information about the flow field and the wave exerted forces on the vegetation by means of a very refined resolution around the cylinders. Additional simulations are carried out with the aim of studying the influence of solitary relative wave height, vegetation density and vegetation arrangement on the tsunami wave attenuation and the forces exerted on the plants. Not only uniform but also random arrangements are considered in order to determine close to nature scenarios.

It is seen from the simulations that the wave induced forces and the wave attenuation due to the rigid vegetation is clearly influenced by the arrangement. Wave damping rates are affected by the relative location of the cylinders, the solid fraction of the patch and the cylinders spacing. It is found that uniform arrangements that are usually tested in laboratory experiments or simulated numerically give reasonable good results according to wave damping. However, large differences are found in the forces exerted on the vegetation for uniform and random distributions. Generalizations obtained from uniform arrangements could lead to underestimation of wave-exerted forces, especially for low dense configurations and the ones found in nature, which follow random arrangements.

The macroscopic approach is able to produce satisfactory results for the prediction of wave height evolution along the patch and the momentum damped by vegetation if the appropriate C_D is found. However, maximum wave-exerted forces on the cylinders are not well reproduced. The differences observed in the numerical results suggest the necessity of using the exact geometry of the plants to correctly address the forces exerted by the flow on the plants. Deviations increase for increasing Reynolds number and wave non-linearity.

Following the macroscopic approach to reduce computational costs requires new C_D formulations. Current formulations were obtained for periodic waves and submerged plants providing results far from the values obtained numerically in this work. It is also detected the strong influence of the vegetation density and the plant arrangement on wave exerted forces on the cylinders. New studies to find appropriate formulations for tsunami waves, which better address the parameterization of the tsunami wave damping by rigid vegetation as mangrove forest need to include the influence of plant arrangements, plant geometry or Reynolds number. Direct simulations with IHFOAM may contribute to better parameterize drag forces in wave models aiming to simulate damping at large scales.

Acknowledgments

M. Maza is indebted to the MEC (Ministerio de Educación, Cultura y Deporte, Spain) for the funding provided in the FPU (Formación del Profesorado Universitario) studentship (BOE-A-2012-6238). This work has been partially funded under the RETOS program of the Spanish Ministry of Economy and Competitiveness.

References

Anderson, M. E. (2010). *Measurements and linear wave theory based simulations of vegetated wave hydrodynamics for practical applications*. Thesis

Chakrabarti, S. K., (1987). *Hydrodynamics of offshore structures*. Computational Mechanics Publications and Springer, New York.

Cheng N.S., Nyugen, H.T. (2011). *Hydraulic radius for evaluating resistance induced by simulated emergent vegetation in open-channel flows*. Journal of hydraulic engineering, 137, 995-1004.

del Jesus, M., Lara, J.L., Losada, I.J. (2012). *Three-dimensional interaction of waves and porous coastal structures Part I: Numerical model formulation*. Coastal Engineering, 64, 57–72.

Dean, R.G., Dalrymple, R.A. (1991). *Water wave mechanics for engineers and scientists*. Advanced Series on Ocean Engineering, 2, World Scientific.

DuPont, S., Gosselin, F., Py, C., de Langre, E., Hemon, P., Brunet, Y. (2010). *Modelling waving crops using large-eddy simulation: comparison with experiments and a linear stability analysis*. J. Fluid Mech., 652, 5 – 44.

Harada, K., Imamura, F. (2003). *Evaluation of tsunami reduction by control forest and possibility of its use for mitigation.* Proc. of Coastal Engineering, Japan Society of Civil Engineers, 341-345. (In Japanese).

Higuera, P., Lara, J.L., Losada, I.J. (2013a). *Realistic wave generation and active wave absorption for Navier–Stokes models: application to OpenFOAM*. Coastal Engineering, 71, 102–118.

Higuera, P., Lara, J.L., Losada, I.J. (2013b). *Simulating coastal engineering processes with OpenFOAM*. Coastal Engineering, 71, 119–134.

Higuera, P., Lara, J.L., Losada, I.J. (2014a). *Three-dimensional interaction of waves and porous coastal structures using OpenFOAM. Part I: formulation and validation.* Coastal Engineering, 83, 243–258.

Higuera, P., Lara, J.L., Losada, I.J. (2014b). *Three–dimensional interaction of waves and porous coastal structures using OpenFOAM. Part II: Applications.* Coastal Engineering, 83, 259–270.

Hiraoka, H., Ohashi, M. (2006). *A (k-ε) turbulence closure model for plant canopy flows*. Proc. of the 4th International Symposium on Computational Wind Eng. (CWE2006) in Yokohama.

Hu, Z., Suzuki, T., Zitman, T., Uittewaal, W., Stive, M. (2014). *Laboratory study on wave dissipation by vegetation in combined current-wave flow*. Coastal Engineering, 88, 131-142.

Huang, Z., Yao, Y., Sim, S.Y. and Yao, Y. (2011). *Interaction of solitary waves with emergent, rigid vegetation.* Ocean Engineering, 38, 1080-1088.

Irtem, E., Gedik, N., Kabdasli, M.S., Yasa, N.E. (2009). *Coastal forest effects on tsunami run-up heights*. Ocean Engineering, 36 313-320.

Ismail, H., Abd Wahab, A.K., Alias, N.E. (2012). *Determination of mangrove forest performance in reducing tsunami run-up using physical models*. Nat. Hazards, 63, 939-963.

Kandasamy, K., Narayanasamy, R. (2005). *Coastal mangrove forest mitigated tsunami.* Estuarine, Coastal and Shelf Science, 65, 601-606.

Koch, D. L., Ladd, A. J. C. (1997). *Moderate Reynolds number flows through periodic and random arrays of aligned cylinders*. Journal of Fluid Mechanics, 349, 31-66.

Ma, G., Kirby, J.T., Su, S.F., Figlus, J., Shi, F. (2013). *Numerical study of turbulence and wave damping induced by vegetation canopies*. Coastal Engineering, 80, 68–78.

Maza, M., Lara, J.L., Losada, I.J. (2013). *A coupled model of submerged vegetation under oscillatory flow using Navier–Stokes equations*. Coastal Engineering, 80, 16-34.

Mazda, Y., Wolanski, E., King, B., Sase, A., Ohtsuka, D., Magi, M. (1997). *Drag force due to vegetation in mangrove swamps*. Mangroves and Salt Marshes, 1, 193–199.

Mazda, Y., Magi, M., Ikeda, Y., Kurokawa, T., Asano, T. (2006). *Wave reduction in mangrove forest dominated by Sonneratia sp*. Wetlands Ecol. Manag., 14, 365-378.

Mei C.C., Chan I.-C., Liu P.L.-F., Huang Z., Zhang W. (2011). *Long waves through emergent coastal vegetation*. J Fluid Mech 461, 461–491.

Mei, C.C., Chan, I.C., Liu, L.-F. P. (2013). *Waves of intermediate length through an array of vertical cylinders.* Environmental Fluid Mechanics, 14, 235-261.

Mendez, F.J., Losada, I.J. (2004). *An empirical model to estimate the propagation of random breaking and non-breaking waves over vegetation fields*. Coastal Engineering, 52, 103 – 118.

Mendez, F.J., Losada, I.J., Losada, M.A. (1999). *Hydrodynamics induced by wind waves in a vegetation field.* Journal of Geophysical Research, 104, 18383-18396.

Menter, F. R. (1992). *Improved Two-Equation k-omega Turbulence Models for Aerodynamic Flows*. NASA TM 103975.

Menter, F.R., (1994). *Two-equation eddy viscosity turbulence models for engineering applications*. AIAA Journal 32 (8), 1598–1605.

Nepf, H. M. (1999). *Drag, turbulence and diffusion in flow through emergent vegetation*. Water Resources Reseach, 5(2), 479-489.

Rusche, H. (2002). *Computational fluid dynamics of dispersed two-phase flows at high phase fractions*. Ph.D. thesis, Department of Mechanical Engineering, Imperial College of Science, Technology & Medicine, London.

Shuto, N. (1987). *The effectiveness and limit of tsunami control forest*. Coastal Engineering in Japan, 30, 143-153.

Strusinska-Correia, A., Husrin, S., Oumeraci, H. (2013). *Tsunami damping by mangrove forest: a laboratory parameterized trees*. Nat. Hazards Earth Syst. Sci., 13, 483-503.

Sumer, B.M., Fredsoe, J. (2006). *Hydrodynamics around cylindrical structures.* Advanced series on ocean engineering, 26.

Suzuki, T., Zijlema, M., Burger, B., Meijer, M.C., Narayan, S. (2011). *Wave dissipation by vegetation with layer schematization in SWAN*. Coastal Engineering. 59, 64-71.

Tanaka, N., Sasaki, Y., Mowjood, M.I.M., Jinadasa, K.B.S.N., Homchuen, S. (2007). *Coastal evegattion structures and their functions in tsunami protection: Experience of the re-cent Indian Ocean tsunami*. Landscape Ecol. Eng., 3, 33-45.

Tanino, Y., Nepf, H. (2008). *Laboratory investigation on mean drag in a random array of rigid, emergent cylinders*. Journal of Hydraulic Engineering, 134, 34–41.

Tanino, Y., Nepf, H. (2009). *Laboratory investigation of lateral dispersion within dense arrays of randomly distributed cylinders ar transitional Reynolds number*. Physics of fluids, 21, 046603-1-046603-10.

Teh, S.Y., Koh, H.L., Liu, P.L.F., Ismail, A.I.M., Lee, H.L. (2009). *Analytical and numerical simulation of tsunami mitigation by mangroves in Penang, Malaysia*. Journal of Asian Earth Sciences, 36, 38-46.

Vo-Luong, H.P., Massel, S.R. (2008). *Energy dissipation in non-uniform mangrove forests of arbitrary depth*. J. Mar. Syst., 74, 603-622.

Weller, H.G., Tabor, G., Jasak, H., Fureby, C. (1998). *A tensorial approach to computational continuum mechanics using object oriented techniques*. Comput. Phys., 12 (6), 620–631.

Wilcox, D. C. (2006). *Turbulence Modeling for CFD.* 3rd edition, DCW Industries, Inc., La Canada CA.